Engineered protein circuits for cancer therapy

Andrew Lu[1,2], Lukas Moeller*[1], Stephen Moore*[3], Shiyu Xia[1], Kevin Ho[1], Evan Zhang[1], Mark W. Budde[4], Haley Larson[1], Ali Ahmed Diaz[1], Bo Gu[1], James M. Linton[1], Leslie Klock[1], Michael J. Flynn[1], Xiaojing J. Gao[5], Daniel J. Siegwart[3], Hao Zhu[3], Michael B. Elowitz[1]†

* These authors contributed equally to this work

[1]Howard Hughes Medical Institute and Division of Biology and Biological Engineering, California Institute of Technology, Pasadena, CA 91125, USA
[2]UCLA-Caltech Medical Scientist Training Program, Los Angeles, CA, USA
[3]Harold C. Simmons Comprehensive Cancer Center, University of Texas Southwestern Medical Center, Dallas, TX, USA
[4]Current address: Plasmidsaurus, South San Francisco, CA, USA
[5]Department of Chemical Engineering, Stanford University, Stanford, CA, USA
† Corresponding author: M.B.E. (melowitz@caltech.edu)

Summary

Many targeted therapies indirectly suppress cancer cells by inhibiting oncogenic signaling pathways such as Ras[1–4]. This renders them susceptible to resistance and limits their long-term clinical efficacy[4–10]. Engineered protein circuits[11–25] have been envisioned as an alternative to pharmacological inhibition that directly rewires oncogenic activity to cell death. However, it has remained unclear whether engineered protein circuits can potently and safely treat cancers. Here, we show that Ras-targeting circuits can accurately discriminate between cancer and non-cancer cells, circumvent intrinsic and acquired resistance mechanisms that limit pharmacological inhibitors, and suppress cancer *in vivo*. These circuits combine three modules: a protease-based sensor that responds to a broad spectrum of clinically relevant Ras mutations, an optional protease amplifier, and protease-triggered cell death effectors. These effectors can flexibly trigger either non-inflammatory apoptosis or immunogenic pyroptosis, which has been shown to extend therapeutic effects beyond transfected cells[26,27]. The resulting sense-kill circuits can be safely, efficiently, and transiently delivered to cells as mRNA in lipid nanoparticles (LNPs). The circuits exhibited potent efficacy against Ras-mutant human cancer cell lines with minimal off-target killing of wild-type Ras cells. In immunocompetent mice bearing aggressive, multifocal Ras-driven liver tumors, intravenously-delivered mRNA-LNP circuits significantly reduced tumor burden. Further, therapeutic circuits provided more potent killing of Ras-mutant cancer cells than the Ras inhibitors Sotorasib and RMC-7977[7,28–30], and exhibited increased sensitivity to Sotorasib-resistant cells *in vitro*. These results establish a potent, specific, and programmable mechanism for treating cancer and other human diseases.

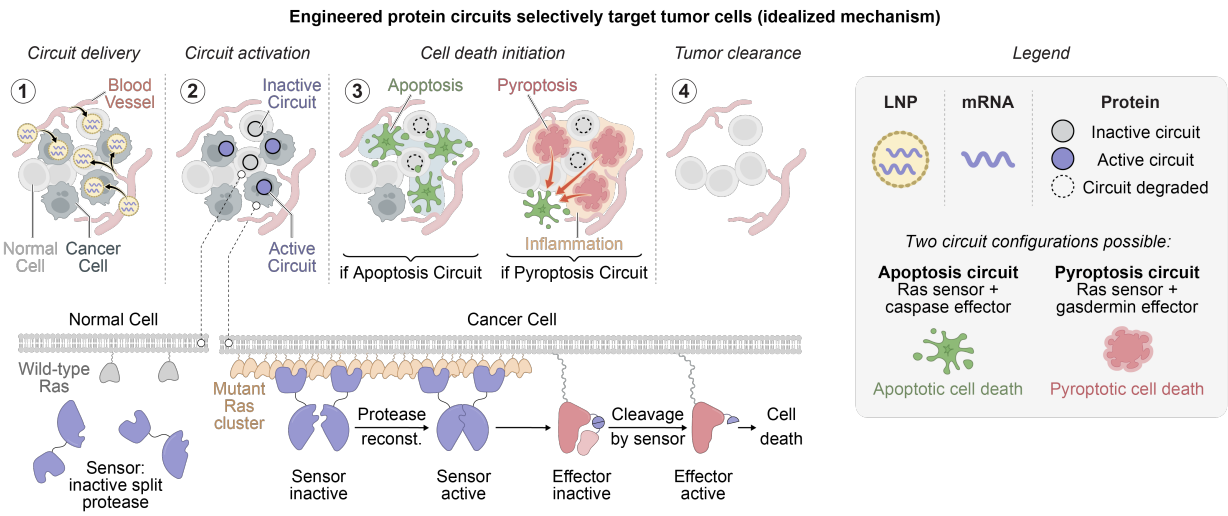

Figure 1. Engineered protein circuits selectively target cancer cells (idealized schematic). (1) Therapeutic circuits composed of sensor and effector modules can be delivered to cells as mRNA in lipid nanoparticles (LNPs). (2) Sensors activate selectively upon binding mutant Ras clusters. More specifically, Ras clustering co-recruits complementary split protease sensor halves to the cell membrane, leading to protease reconstitution (lower panel). (3) Active sensors trigger cell-death effectors and initiate apoptotic (left) or pyroptotic (right) cell death in Ras-mutant cells. Pyroptosis could further stimulate the immune system to kill non-transfected cells (arrows). (4) Circuits eliminate Ras-driven tumors without harming healthy tissue.

Main

Therapeutic circuits comprise sets of engineered proteins that can be expressed in cells to sense disease-specific signals and conditionally trigger cell death or other responses (**Figure 1**). In the context of cancer, they have the potential to offer higher efficacy and less opportunity for resistance than targeted therapies[4,15], greater molecular specificity than chemotherapies[31,32], and an expanded ability to sense intracellular proteins compared to CAR-T cells[33,34] and antibody-drug conjugates[35,36]. While aspects of the therapeutic circuit paradigm have been explored[11–15,17,37–44], fundamental questions have remained: Can engineered proteins sensitively and specifically detect mutant oncogenes in cancer cells? Can therapeutic circuits treat tumors *in vivo*? And, how do therapeutic circuits compare to targeted small molecule drugs in terms of treatment efficacy and resistance?

Here, we describe the design, optimization, and characterization of protease-based therapeutic circuits that selectively kill Ras-mutant cancer cells. Proteases represent ideal building blocks for therapeutic circuits. They are modular, engineerable and can directly interface with endogenous pathways[11,13,46–48]. We target Ras because Ras mutations drive roughly one in four human cancers, yet durable and effective Ras-targeting therapies remain limited[2,7,45]. More specifically, we develop sensitive and broadly specific protease-based sensors of mutant Ras, engineer a protease-activated protease module that amplifies signals, and couple sensors and amplifiers to cell death effectors. Delivered as mRNA in lipid nanoparticles (LNPs), these circuits can target Ras-driven cancer cells *in vitro* as well as Ras-driven liver tumors *in vivo*. Finally, we demonstrate that therapeutic circuits can provide advantages in efficacy and resistance compared to two state-of-the-art targeted pharmacological Ras inhibitors.

Engineered sensors specifically respond to diverse Ras mutations

An ideal Ras sensor should strongly activate in the presence of diverse oncogenic Ras mutants, but not respond to wild-type Ras. A previous sensing mechanism used Ras binding domains attached to complementary halves of a split Tobacco Etch Virus (TEV) protease[13,14]. Ras activation could then recruit split sensor proteins to Ras clusters, leading to protease reconstitution (**Figure 2a**). In its initial design (*v1)*, the sensor used the natural Ras-binding domain of RAF1. Despite responding to overexpressed Ras in HEK293 cells, this *v1* sensor poorly discriminated mutant and wild-type Ras variants, due to limited specificity and undesired sensor multimerization (**Extended Data Figure 1**).

We hypothesized that more specific and higher-affinity Ras binding domains could improve sensor function. To identify domains that would enable broad-spectrum mutant Ras sensing, we constructed a comprehensive library of human, *de novo* designed, and synthetic Ras binders. Specifically, we compiled a set of candidate human Ras binders by selecting proteins known to associate with KRAS, co-folding them with KRAS using AlphaFold3, and filtering for domains with high-confidence KRAS binding interfaces (**Methods**). We also used RFdiffusion to design sensor variants that incorporate *de novo* Ras binders (**Methods**). Finally, we incorporated previously described Ras-binding monobodies[49], designed ankyrin repeat proteins (DARPins)[50,51], synthetic proteins[52], and nanobodies[53]. To screen this library, each of these Ras binding domains was fused with complementary split TEVP domains and co-expressed with a panel of Ras variants as well as a fluorescent protease reporter in HEK293 cells[54] (**Figure 2b**, **Methods**). The reporter used a cleavage-activated IFP to measure protease activity and a GFP to track reporter expression, with the IFP/GFP ratio serving as normalized reporter readout. In the assay, additional fluorescent proteins were co-transfected to enable quantitative flow cytometry scanning of a broad, multi-dimensional expression space for each Ras mutant and candidate sensor (**Figure 2b**, **Extended Data Figure 2a**).

Candidate sensors varied in their responses to mutant ($KRAS^{G12C}$) and wild-type ($KRAS^{WT}$) Ras (**Figure 2c-d**, **Extended Data Figure 2b-c**, **Extended Data Figure 3a-c**). Among the *de novo* designed binders, a small subset exhibited weak discrimination of mutant over wild-type Ras, providing a basis for potential further optimization (**Extended Data Figure 3b**). Sensors based on the synthetic monobody NS1 or the DARPins K13 and K19 were strongly Ras-responsive but did not discriminate between wild-type and mutant Ras variants (**Figure 2c-d**). By contrast, sensors based on the previously described 12VC synthetic monobody (12VC1 and 12VC3) achieved sensitive and specific discrimination of mutant and wild-type Ras (**Figure 2c-d**). This likely reflects the monobody selection process, which combined positive selection for $KRAS^{G12C}$ binding with negative-selection against wild-type KRAS. Further, the 12VC1 sensor—henceforth referred to as *v2*—exhibited a sensor expression-dependent response across a broad range of Ras expression levels (**Figure 2d**, **Extended Data Figure 4b**).

The *v2* sensor detected a broad spectrum of clinically relevant oncogenic Ras variants. Following a similar experimental procedure as described above (**Methods**), we analyzed the response of *v2* to a panel of 46 prevalent KRAS, HRAS, and NRAS mutations from the TCGA database[55,56]. At matched Ras expression levels, the *v2* sensor strongly responded to most KRAS, HRAS, and NRAS mutants (**Figure 2e**, **Extended Data Figure 4a**). The prevalent G12 mutations G12C, G12V, G12S, and G12A induced strong responses (**Figure 2e**). Notably, the v2 sensor produced sufficient discrimination of

wild-type and mutant Ras-expressing cells to enable accurate classification at the single-cell level (**Figure 2f**, **Extended Data Figure 4c**).

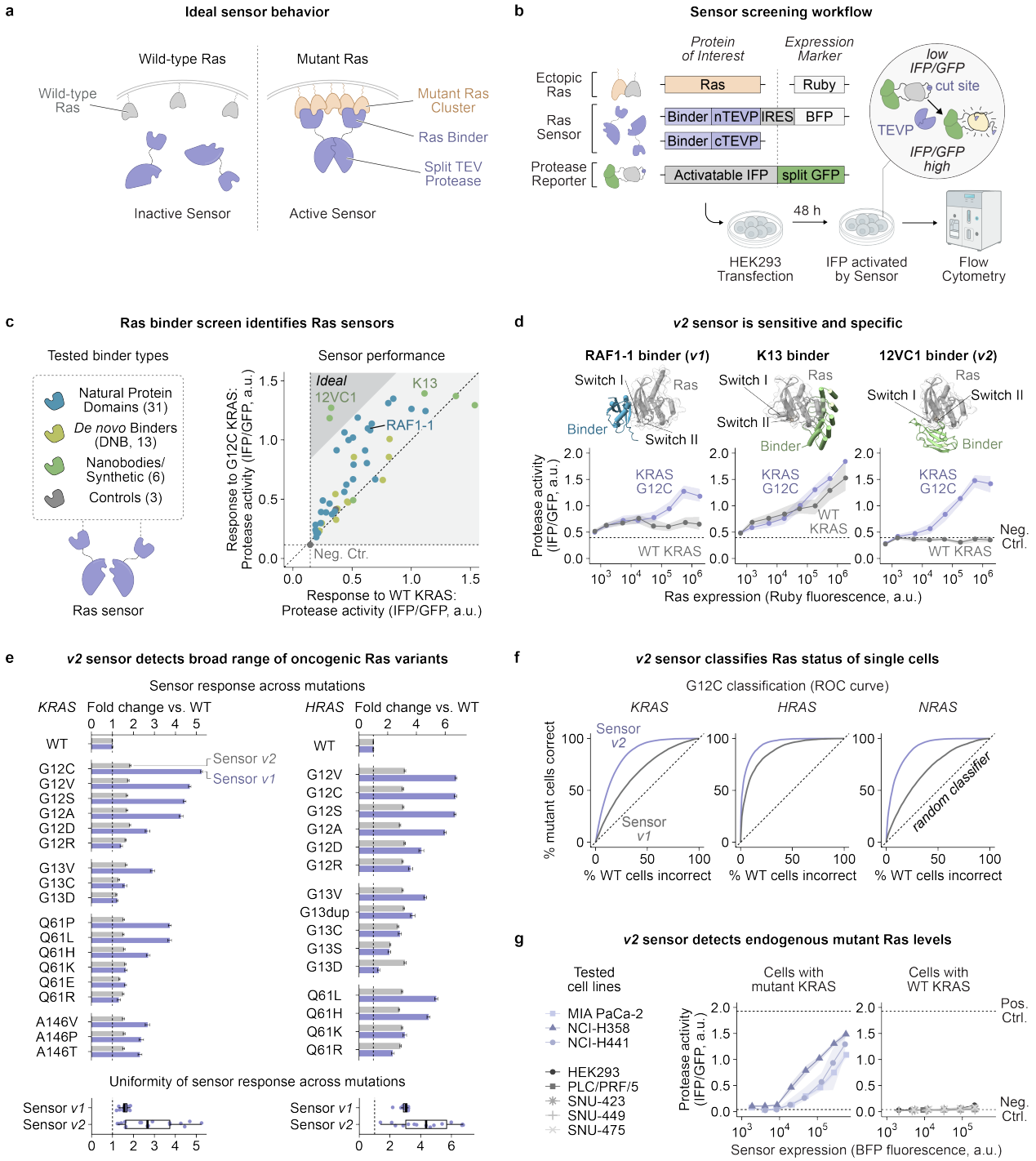

Figure 2. Engineered sensors specifically respond to mutant Ras.

a, An ideal sensor should reconstitute a split protease effector in response to mutant but not wild-type Ras. **b**, To screen for sensitive and specific Ras sensors, HEK293 cells were transiently transfected with ectopic Ras variants (marked by mRuby3), candidate sensors (marked by mTagBFP2, labeled BFP), and a protease-activatable fluorescent reporter (IFP/GFP ratio denotes reporter activation). This setup enabled quantitative

analysis of sensor performance across a multi-dimensional space of sensor and Ras expression levels. **c**, The responses of candidate Ras sensors were characterized against mutant ($KRAS^{G12C}$) and wild-type Ras ($KRAS^{WT}$). Data points represent median reporter activation in high Ras expression regimes (**Methods**). Sensors are color-coded by the type of Ras binding domain (legend). Horizontal and vertical dotted lines denote reporter activation in the absence of a sensor (negative control). **d**, Sensor *v2* (12VC1-based) maintains high sensitivity to mutant Ras across a broad range of ectopic Ras expression levels, with minimal background activation in wild-type Ras-expressing cells. Data points represent median reporter activation (**Methods**). Negative control line represents the activity of a sensor containing GSGSGS peptides as binders. Structures depict binders in complex with KRAS (RAF1-1: structure generated by AlphaFold3, K13: structure from PDB entry 6H46[50], 12VC1: structure from PDB entry 7L0G[53]). **e**, *Top*: *v2* (purple) exhibits enhanced sensitivity to a wide range of oncogenic KRAS (left) and HRAS (right) mutations compared to *v1 (*gray). Bars show the fold-change sensor activation in response to mutant relative to wild-type Ras after gating for high Ras expression (**Methods**). *Bottom*: *v1* exhibited more uniform response to diverse Ras mutations compared to *v2*. Data points correspond to the fold-change sensor activation to mutant relative to wild-type Ras. Boxplots show median (center line), quartiles (box), and 1.5x interquartile range (line). Dotted line corresponds to equal responses to mutant and wild-type Ras. **f**, At the single-cell level, the *v2* sensor discriminated between mutant and wild-type Ras-expressing cells. Receiver operating characteristic (ROC) analysis was performed by varying the protease reporter threshold, generating a confusion matrix, and plotting the true positive rate (Ras-mutant cells above reporter threshold) against the false positive rate (wild-type Ras cells above reporter threshold) at matched Ras expression levels. Dotted line represents the performance of a random classifier. **g**, *v2* sensor detects endogenous mutant Ras levels. Sensors and fluorescent protease reporter were transiently transfected into cancer cell lines with endogenous levels of Ras and analyzed by flow cytometry. The human cancer cell lines MIA PaCa-2 ($KRAS^{G12C}$), NCI-H358 ($KRAS^{G12C}$), and NCI-H441 ($KRAS^{G12V}$) express mutant Ras, while HEK293, PLC/PRF/5, SNU-423, SNU-449, and SNU-475 express wild-type KRAS. Negative control line represents the activity of a sensor containing GSGSGS peptides as binders. Positive control line represents a sensor containing the P3/P4 coiled-coiled domains as binders. Error bars and shaded error regions in panels **d**, **e**, and **g** were computed as bootstrap 95% confidence intervals of the median (**Methods**). **c**, **d**, **e, f** were computed in cells with intermediate sensor expression levels.

To evaluate v*2* sensor activity at physiologic Ras expression levels, we transfected human cancer cell lines with the sensor and a protease reporter. The sensor strongly responded in cell lines with mutant Ras, including MIA PaCa-2 ($KRAS^{G12C}$), NCI-H358 ($KRAS^{G12C}$), and NCI-H441 ($KRAS^{G12V}$; **Figure 2g**). By contrast, it showed minimal response in cancer cell lines with wild-type Ras, including PLC/PRF/5, SNU-423, SNU-449, SNU-475. Taken together, these results indicate that the *v2* sensor can sensitively and specifically respond to diverse, clinically-relevant Ras mutants expressed at endogenous levels in human cells.

Sensor optimization and signal amplification improve sensitivity

Anticipating variability of *in vivo* delivery, we redesigned the two-protein sensor as a single gene construct (**Figure 3a**). First, we tried incorporating a T2A-P2A ribosomal skipping sequence. However, this modification degraded sensor performance (**Figure 3b**). As an alternative, inspired by natural self-cleaving viral polyproteins[57], we introduced intramolecular cleavage sites for the sensor protease itself. In these designs, a polyprotein containing both sensor protein halves post-

translationally cleaves itself into the two sensor components. These self-cleaving designs increased maximal activation. Additionally, incorporating TEV protease mutations[58,59] further enhanced sensitivity (**Figure 3b**). Based on these results, we adopted the self-cleaving sensor *v2-s* for subsequent experiments.

We also explored signal amplification as a complementary approach to enhance sensor performance. Inspired by amplifying proteolytic cascades in cell death pathways[60,61], we engineered synthetic protease-activatable proteases (**Extended Data Figure 5**) using the tobacco vein mottling virus protease (TVMVP), which is orthogonal to the TEV protease. In the best design, split TVMVP halves were fused to caging domains consisting of catalytically dead complementary protease halves, which could be removed through TEVP cleavage (**Figure 3c**). Once cleaved by TEVP, active TVMVP halves can reconstitute via attached coiled-coiled domains (**Methods**). This double-caged system amplified input signals compared to a constitutive TEVP alone, while maintaining minimal background activity in the absence of input TEVP signals (**Figure 3d**). Together, these results establish optimized sensors and amplifiers for downstream *in vivo* applications.

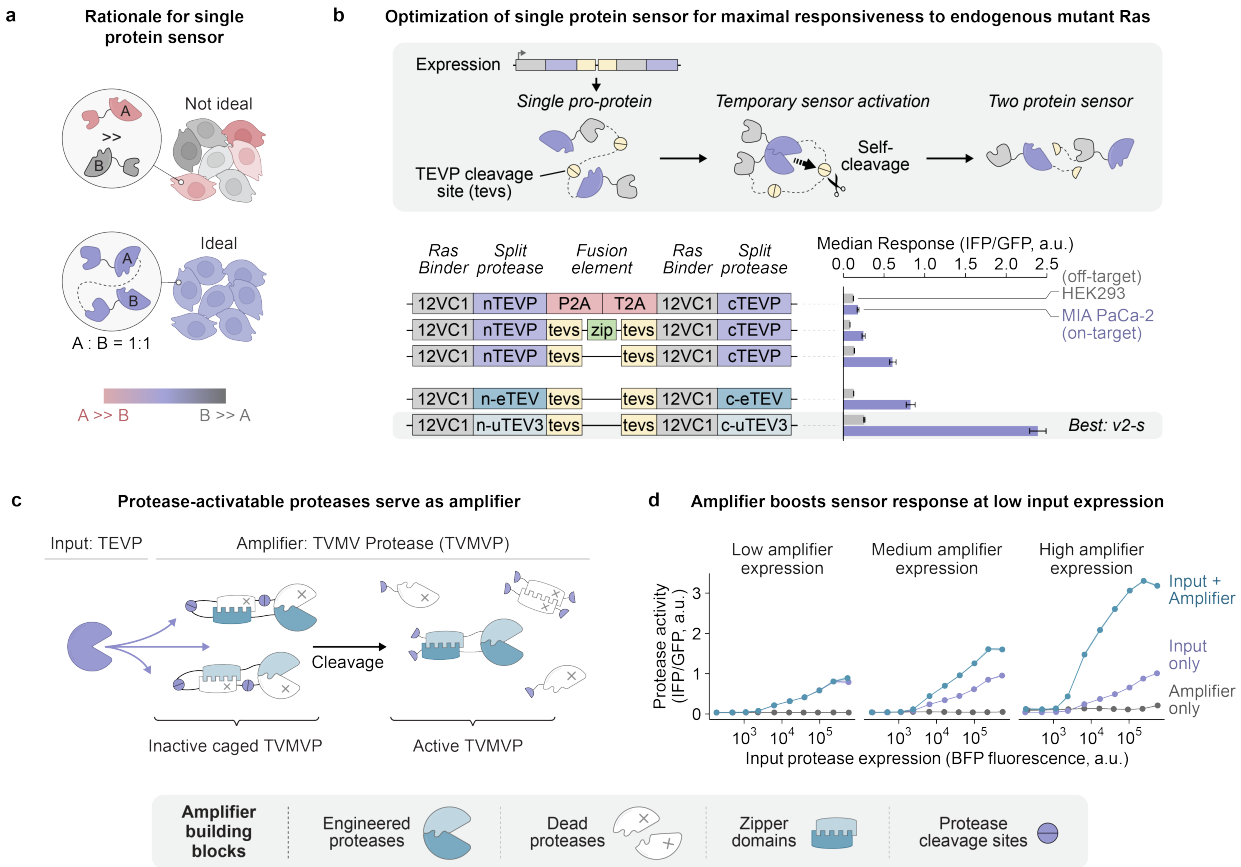

Figure 3. Cis and trans protease regulation increases sensitivity

a, Single-protein sensor designs facilitate 1:1 stoichiometry between sensor components to improve sensor performance. **b**, Sensor *v2-s* improves mutant Ras discrimination through "self-cleaving" mechanism (cis regulation) inspired by natural viral mechanisms. Some sensor designs incorporated mutant TEV protease variants (eTEV, uTEV3) with elevated catalytic efficiencies[58,59]. Median sensor responses (IFP/GFP ratio)

were measured in on-target (KRAS^{G12C}-expressing MIA PaCa-2) and off-target (wild-type KRAS-expressing HEK293) cells. **c**, Amplifier proteases (TVMVP) can be activated by TEVP cleavage. In this design, both halves of split TVMVP are fused to their complementary, catalytically dead halves and held together by a weak coiled-coil interaction, thus intramolecularly caging and inhibiting TVMVP activity. Cleavage by TEVP removes the inactive fragments, allowing the active halves to displace the weak interaction with a stronger coiled-coil pair, reconstituting TVMV protease. **d**, Protease amplifier increases output compared to non-amplified circuits when expressed at different levels (individual plots). Response curves are shown across low (gating for co-transfected Ruby between 10^3-10^4 a.u.), medium (10^4-10^5 a.u.), and high (10^5-10^6 a.u.) amplifier expression bins.

Circuits potently and selectively eliminate Ras-mutant cancer cells

To enable selective cancer cell killing in response to mutant Ras sensing, a complete therapeutic circuit must (1) be efficiently delivered to both healthy and cancer cells, and (2) couple Ras sensors to tightly controlled effectors of cell death. We confirmed that an existing LNP formulation[62,63] could efficiently deliver *in vitro* transcribed mRNA to human cells in culture, and that protein expression levels are quantitatively tunable by LNP concentrations (**Extended Data Figure 6a-b**, **Methods**).

We first couple mutant Ras sensors to effectors of apoptosis, a precise and tightly regulated mode of cell death. Specifically, we separately encapsulated mRNAs encoding the *v2-s* sensor and a TEVP-activatable, membrane-localized caspase-3 effector (Casp-3) that conditionally triggers apoptosis (**Figure 4a**). We delivered different concentrations of the two mRNA-LNP components to human cancer cell lines and analyzed cell viability 3-5 days post-treatment. Both the sensor and the effector were well tolerated across a wide dosage regime when delivered individually (**Figure 4b-c**). Strikingly, co-delivery of the sensor and caspase effector induced potent, near-complete, and dose-dependent killing in Ras-mutant cancer cell lines, while sparing Ras wild-type cells (**Figure 4b-c**). These results demonstrate that therapeutic circuits can selectively kill human Ras-mutant cancer cells.

To broaden the effects of therapeutic circuits beyond transfected cells, we also coupled Ras sensing to effectors of pyroptosis, an immunogenic form of cell death. Indeed, current mRNA delivery methods cannot penetrate all tumor cells *in vivo*. While partial tumor clearance may offer some therapeutic benefit, extending circuit-mediated killing to non-transfected cancer cells would be advantageous. Unlike apoptosis, pyroptosis releases inflammatory cytokines that can recruit the immune system, inducing non-cell autonomous tumor clearance even when triggered in a minority of cancer cells[26,27] (**Figure 1**). To test conditional activation of pyroptosis, we co-delivered the *v2-s* Ras sensor with a cleavage activatable gasdermin, the natural cell death effector of the pyroptosis program. As above, these components induced negligible background cell death when delivered alone, but potently and selectively eliminated Ras-mutant human cancer cells when co-delivered as a complete therapeutic circuit (**Figure 4b**). Together, these results show that therapeutic circuits delivered as mRNA in LNPs can effectively target Ras-mutant cancer cells with two complementary cell death programs.

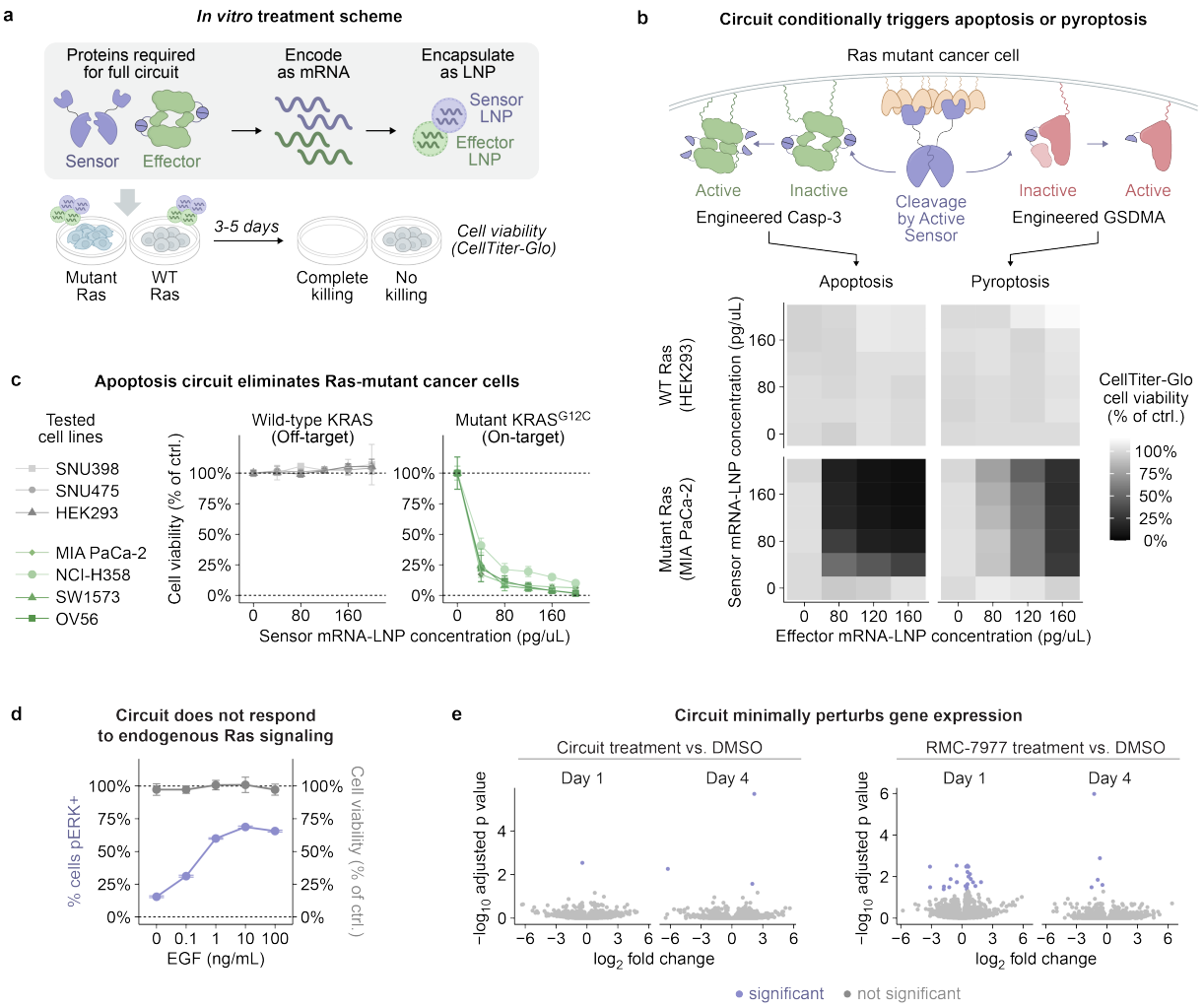

Figure 4. Therapeutic circuits potently and selectively eliminate Ras-mutant cancer cells.
a, *In vitro* treatment scheme for therapeutic circuits. mRNA-encoded sensors and effectors were encapsulated in lipid nanoparticles (LNPs) and delivered to cancer cells. Cell viability was measured 3-5 days post-treatment using CellTiter-Glo. **b**, Engineered sensor *v2-s* conditionally activates apoptosis (via engineered Casp-3) or pyroptosis (via engineered Gasdermin A, GSDMA) effectors in cells harboring mutant Ras. Heatmaps show selective killing of mutant Ras-expressing (MIA PaCa-2) vs. wild-type (HEK293) cells across different sensor and effector mRNA-LNP concentrations ($n = 3$ replicates, mean cell viability depicted). **c**, Circuit composed of sensor *v2-s* and engineered Casp-3 selectively eliminates cancer cells harboring mutant Ras (MIA PaCa-2, NCI-H358, SW1573, OV56; all $KRAS^{G12C}$), but spares wild-type Ras-expressing control cell lines (SNU398, SNU475, HEK293; all $KRAS^{WT}$). Viability expressed as luminescence normalized to no sensor controls; error bars represent mean ± sd ($n = 3$ replicates). **d**, Circuit responsiveness to endogenous Ras signaling induced by EGF stimulation. Ras activation was quantified as the percentage of pERK-positive cells measured by antibody staining and flow cytometry. Error bars for pERK measurements represent 95% confidence intervals derived from bootstrapping (1,000 iterations). Cell viability was assayed with CellTiter-Glo; error bars represent mean ± sd ($n = 2$ replicates). **e,** RNA-seq on HEK293 cells treated with RMC-7977 or circuit at day 1 or day 4 post-treatment.

Circuits do not respond to endogenous Ras signaling or perturb gene expression

A potential safety concern is off-target activation of circuits in wild-type cells engaged in normal Ras signaling. To test for such effects, we transfected mRNA-LNP circuits in HEK293 cells with or without Ras stimulation by epidermal growth factor (EGF). EGF treatment rapidly induced activation of the RAS-MEK-ERK pathway[64], with ERK phosphorylation detectable within 15 minutes, as expected[65] (**Figure 4d**). Nevertheless, the transfected cells exhibited no detectable cell death, even at saturating EGF concentrations. This ability to discriminate between wild-type and mutant Ras signaling may reflect a difference in Ras activation dynamics, with cancer cells exhibiting more sustained Ras activity than wild-type cells, where activation may be adaptive or oscillatory[64,66,67]. These results demonstrate a safety feature of the sense-kill circuits and help explain their mutant specificity.

Another potential safety concern is that transient expression of circuit components could potentially perturb cell states. Using RNA-seq, we analyzed the gene expression profile of HEK293 cells following treatment with either the mRNA-LNP circuit or the Ras targeting inhibitors Sotorasib and RMC-7977. 24h after treatment, the mRNA-LNP circuit yielded only one differentially expressed gene (Benjamini-Hochberg-adjusted $p < 0.05$; **Figure 4e**, **Extended Data Figure 6c**). By contrast, RMC-7977 and Sotorasib differentially regulated 24 and 6 genes, respectively. In particular, RMC-7977 downregulated known transcriptional targets of the RAS-MAPK pathway such as DUSP6 ($p = 0.0041$) or ETV5 ($p = 0.003$), consistent with previous results[29] and its role as a pan-Ras signaling inhibitor, while the circuit did not significantly affect these genes. By 4 days post-treatment, gene expression in all three conditions had largely returned to baseline. These results suggest that mRNA-LNP circuits minimally perturb healthy cells.

Circuits prevent and treat induced liver tumors *in vivo*

Having demonstrated specific targeting in cell culture, we next asked whether therapeutic circuits could function *in vivo*. The liver represents an ideal context to test circuits *in vivo* for two reasons. First, existing LNP formulations can efficiently transfect the liver[62,68,69]. Second, the liver is the primary metastatic site for many Ras-driven cancers with high unmet clinical need[70–72], as well as the primary site for Ras-driven cholangiocarcinomas[73].

Liver tumors develop in complex microenvironments, with vasculature, immune cells, and extracellular matrix influencing cancer growth. To recapitulate these features, we used an established autochthonous liver cancer model in immunocompetent mice. In this model, hydrodynamic tail vein injection (HDT) is used to transfect hepatocytes with DNA encoding the oncogenic $NRAS^{G12V}$ Ras variant, an shRNA targeting TP53 (shTP53), and the Sleeping Beauty (SB100) transposase for stable genomic integration and sustained expression. The model generates aggressive and multifocal liver cancers that advance to late-stage disease within five weeks after induction[74–76].

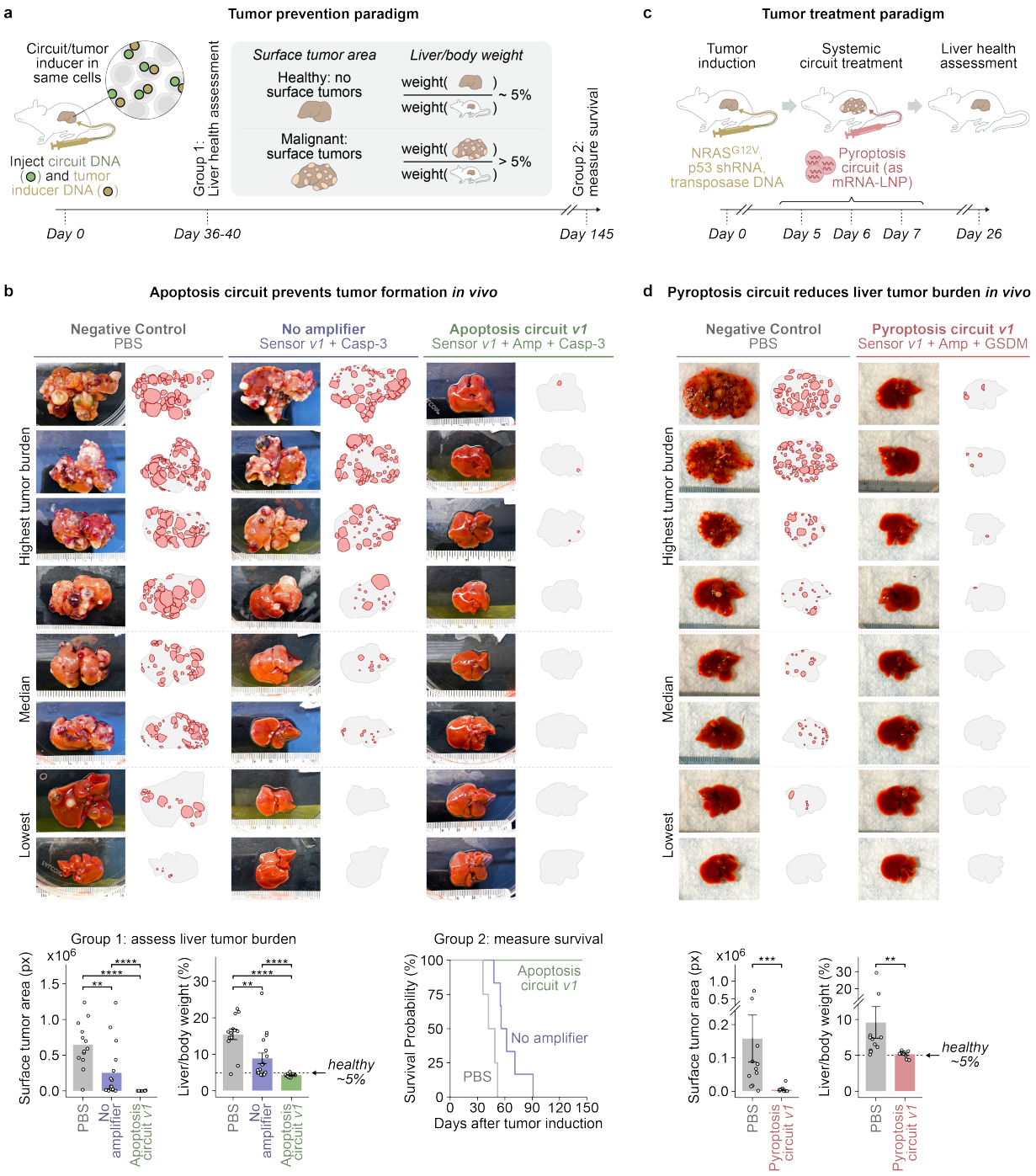

Figure 5. Therapeutic circuits prevent and treat liver tumors *in vivo*.

a, Circuit composed of *v1* sensor, amplifier, and engineered Casp-3 prevents tumor formation *in vivo*. Tumors were generated by co-administration of plasmids encoding NRAS^{G12V}, TP53 shRNA, and a sleeping beauty transposase via hydrodynamic tail vein injection (HDT). Liver tumor burden was quantified using two independent metrics: (1) surface tumor area, manually annotated following blinded evaluation, and (2) liver-to-body weight ratio, a standard quantitative measure in hydrodynamic liver tumor models. **b**, *Top*: mouse livers (n = 13-16 female mice per condition) extracted 36-40 days after tumor induction. Liver images and manually annotated surface tumor nodules (red) are displayed side-by-side. *Bottom left*: quantification of total surface tumor area (blinded manual annotation of tumor nodules). Bars depict mean tumor surface area (px) ± se (error bars). Individual data points denote accumulated surface tumor area of individual animals from

anterior and posterior views. Adjusted p value = 4.1×10^{-3} for PBS vs. no amplifier; 3.2×10^{-6} for PBS vs. full circuit; 3.2×10^{-6} for no amplifier vs. full circuit (pairwise Mann-Whitney U tests with Benjamini-Hochberg (BH) correction). *Bottom middle:* bars depict mean liver/body weight ratio (%) ± se (error bars). Data points denote liver/body weight ratio of individual animals. Adjusted p value = 2.8×10^{-3} for PBS vs. no amplifier; 3.5×10^{-7} for PBS vs. full circuit; 1.5×10^{-5} for no amplifier vs. full circuit (pairwise Mann-Whitney U tests with BH correction). *Bottom right:* overall survival depicted as Kaplan-Meier curves (group 2; n = 7-10 male mice per condition). Median survival 42 days for PBS; 59 days for no amplifier; 145 days (termination of experiment) for full circuit. P value = 7×10^{-4} (***) for PBS vs. no amplifier; 1×10^{-4} (****) for PBS vs. full circuit; 1×10^{-4} (****) for no amplifier vs. full circuit (log-rank test, all p values significant after Bonferri correction). **c**, *In vivo* treatment scheme for therapeutic circuits. mRNA-encoded sensors and effectors were encapsulated in lipid nanoparticles (LNPs) and intravenously administered on days 5, 6, and 7 following tumor induction. On day 26, mice were sacrificed and livers were collected for evaluation of tumor burden. **d**, Systemic intravenous delivery of pyroptosis circuit *v1* (*v1* sensor, amplifier, sensor-activatable gasdermin D; GSDMD) induced robust anti-tumor activity (n = 10-11 female mice per condition). P value = 0.00055 when comparing distribution of surface tumor areas between PBS and circuit *v1*; 0.00078 when comparing distribution of liver/body weight ratios (Mann-Whitney U test). Bars depict mean ± se (error bars). Individual data points denote mean surface tumor area (px) and liver/body weight ratios (%), respectively.

Using this model, we first asked whether circuits could function *in vivo,* independently of potential delivery limitations. To address this question, DNA-encoded circuits were co-administered with the tumor-inducing agents to allow tumor initiation and circuit expression to occur largely in the same liver cells (**Figure 5a**). We used circuits that incorporated the *v1* sensor, as experiments were conducted before the improved sensor variants were developed, and the apoptosis cell death effector, as tumor induction was largely restricted to circuit-expressing cells. Further, we included circuit variants with or without the amplifier. In one mouse cohort, we let tumors develop for five weeks, terminated the experiment, and measured total surface tumor areas and liver-to-body weight ratios, a standard measure of tumor burden in hydrodynamic liver tumor models (**Figure 5a**, **Methods**). In a separate mouse cohort, we tracked survival to determine the durability of tumor suppression (**Figure 5a**, **Methods**).

Mice that received no treatment showed robust, multifocal tumor formation (**Figure 5b**, **Extended Data Figure 7**). Co-delivery of the sensor and cell death effector significantly, but incompletely, reduced tumor burden, as assessed by total surface tumor area ($p = 4.1 \times 10^{-3}$) and liver-to-body weight ratios ($p = 2.8 \times 10^{-3}$; **Figure 5b**, **Extended Data Figure 7**, **Extended Data Figure 8a-b**). The same condition extended median survival from 42 days (in untreated animals) to 59 days ($p = 7 \times 10^{-4}$), but did not eliminate tumor development (**Figure 5b**). Remarkably, inclusion of the amplifier module transformed this partial response into near-complete tumor suppression. Mice that received the complete sense-amplify-kill circuit showed no detectable surface tumors and exhibited liver-to-body weight ratios comparable to those of healthy animals (**Figure 5b**, **Extended Data Figure 7**, **Extended Data Figure 8a-b**). In the parallel cohort, all mice treated with the sense-amplify-kill circuit survived beyond 145 days, at which time the experiment was terminated (**Figure 5b,** $p = 1 \times 10^{-4}$ for comparison to untreated). Overall, these results demonstrated that co-delivered therapeutic circuits can prevent the formation of induced mouse liver tumors *in vivo*.

We next considered a more challenging treatment scenario (**Figure 5c**). Rather than co-delivering circuits with tumor-initiating agents, we initiated tumor formation (day 0) using the same procedure as

above, and then allowed tumors to develop for five days before systemically administering the therapeutic circuits as mRNA-LNP in three doses, on days 5, 6, and 7. On day 25, we sacrificed mice and harvested livers for further analysis. In this case, because the circuits are unlikely to be delivered to the majority of cancer cells, we replaced the apoptosis effector with the pyroptosis effector as output. Thus, the circuits in this experiment consisted of the *v1* sensor, amplifier, and gasdermin pyroptosis effector.

Compared to PBS-treated mice, circuit-treated animals showed near-complete tumor clearance (**Figure 5d**, **Extended Data Figure 8c-d**, **Extended Data Figure 9**). In fact, the livers of circuit-treated animals were almost completely free of surface tumor nodules (p value = 0.00055 compared to the negative control group). The treated animals also exhibited liver-to-body weight ratios comparable to those of healthy animals (p value = 0.00078 compared to negative control group). Thus, circuits delivered systemically using mRNA-LNPs are capable of eliminating previously initiated Ras-driven mouse liver tumors. This result was particularly striking given that this multifocal cancer model is known to be challenging to treat[76], and that this result was obtained using the less optimized sensor.

Circuits kill drug-resistant cells

Both intrinsic and acquired resistance can limit the efficacy of Ras inhibitors (**Figure 6a**). Intrinsic resistance occurs when cancer cells do not exhibit oncogene addiction, and can be assayed by the initial response of Ras-mutant cells to treatment[77]. In contrast, acquired resistance arises when initially sensitive cells adapt over time, either by losing Ras dependency or by activating compensatory pathways to circumvent Ras inhibition[8,77,78]. This form of resistance can be observed through the gradual emergence of resistant cells after extended treatment[79]. We reasoned that therapeutic circuits, by directly rewiring mutant Ras sensing to cell death, could provide fewer opportunities for both types of resistance (**Figure 6a**). To test this hypothesis, we directly compared the performance of the mRNA-LNP-delivered apoptosis circuit (*v2-s* sensor, caspase effector) to two clinically relevant small-molecule Ras inhibitors: Sotorasib, an approved $KRAS^{G12C}$ inhibitor[6,28], and RMC-7977, a pan-Ras inhibitor with a related molecule currently under clinical evaluation[7,29].

To assay for intrinsic resistance, we compared the responses of $KRAS^{G12C}$-mutant MIA PaCa-2 cells to either circuit or drugs. Sotorasib and RMC-7977 reduced cell viability in a dose-dependent manner by up to 74.8±0.5% or 86.8±0.3%, respectively, but neither drug achieved complete cell elimination, even at saturating concentrations (**Figure 6b**). In contrast, the circuit achieved near complete elimination of all cells (97.1±0.1%, **Figure 6b**). The circuit was insensitive to initial cell plating densities, which diminished the potency of the small molecule drugs (**Extended Data Figure 10a**). We further used microscopy to compare drug and circuit effects on co-cultured target (MIA PaCa-2) and non-target (Ras wild-type HEK293) cells, engineered to stably express GFP and mRuby3 markers, respectively. Five days after treatment, the chemotherapeutic agent Paclitaxel produced potent but incomplete and non-specific clearance of both cell types (**Figure 6c**). Sotorasib and RMC-7977 disproportionately reduced the size of the Ras-mutant cell population, but failed to eliminate them entirely, leaving behind visible colonies of Ras-mutant cells (**Figure 6c**). By contrast, the circuit completely cleared Ras-mutant, but not wild-type Ras cells (**Figure 6c**). Together, these results suggest that circuits can be more potent and specific than targeted therapies and chemotherapy.

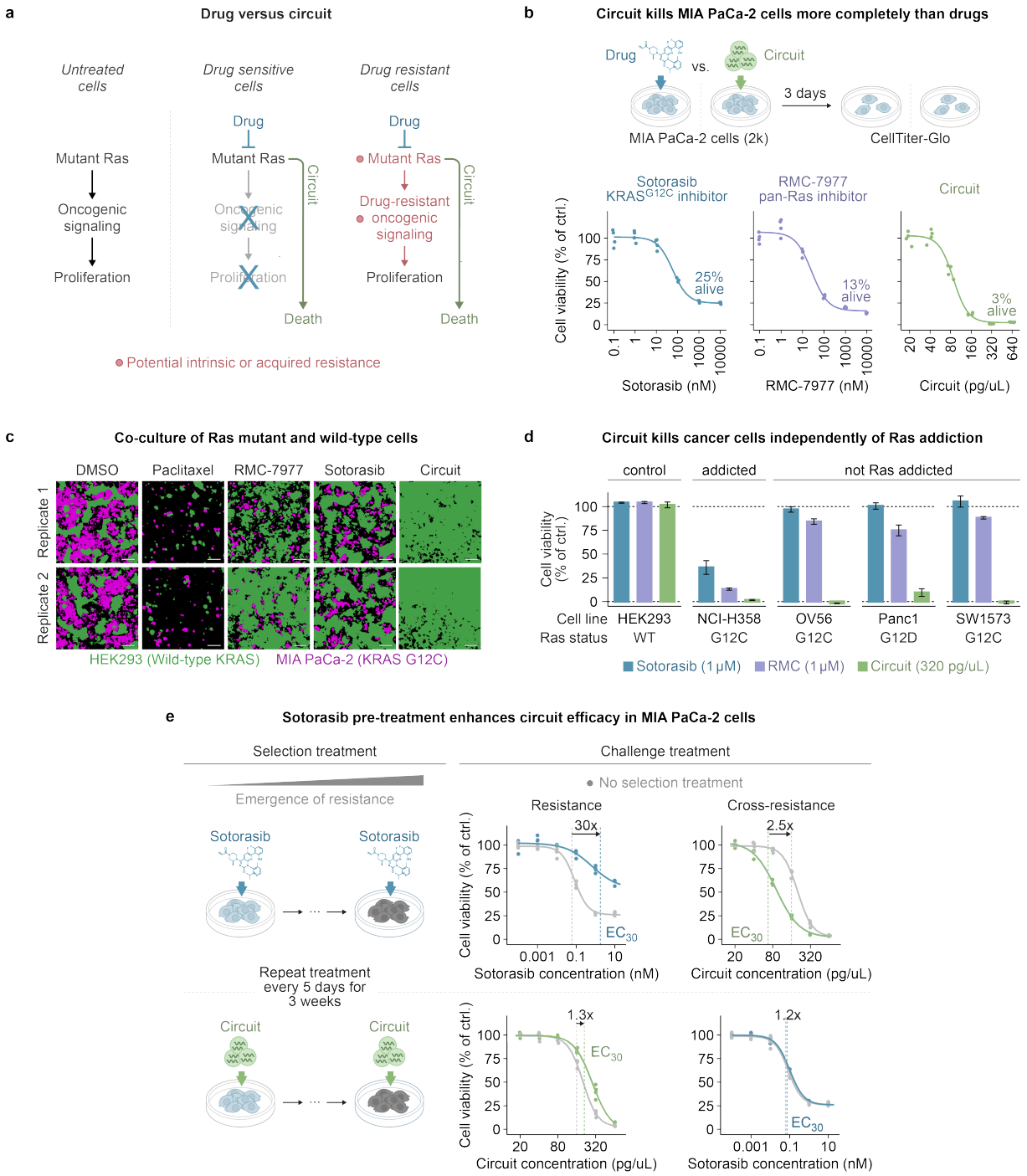

Figure 6. Circuits are less susceptible to intrinsic and acquired resistance compared to Ras-targeting drugs.

a, Circuits can directly induce cancer cell death, potentially minimizing susceptibility to resistance mechanisms that limit targeted therapies. Circuits used in this figure were composed of sensor *v2-s* and Casp-3. If not specified otherwise, circuit concentrations denote accumulated amounts of sensor *v2-s* and Casp-3 added at a 1:1 ratio. **b**, Dose-response curves for Ras inhibitors (Sotorasib, RMC-7977) and circuit. Viability measured after 3 days (CellTiter-Glo, mean ± sd, n = 3-4). Curves were fitted with a four-parameter log-logistic model (**Methods**). **c**, Co-culture of MIA PaCa-2 ($KRAS^{G12C}$) and HEK293 (wild-type KRAS) cells stably expressing GFP and mRuby3, respectively. Cells were treated with saturating concentrations of Paclitaxel (30 μM), RMC-7977 (1 μM), Sotorasib (1 μM), or the therapeutic circuit (150 pg/μL Casp-3 and 100 pg/μL

sensor *v2-s*). Fluorescence images were acquired on day 5. Scale bar, 200 μm. **d**, Efficacy comparison between circuits and Ras inhibitors in cell lines that differ in Ras addiction. Dashed lines represent 0% and 100% cell viability, respectively. **e**, Repeated exposure to Sotorasib or the therapeutic circuit alters subsequent treatment responsiveness in MIA PaCa-2 cells. Cells were treated every 5 days for 3 weeks, then challenged with both Sotorasib and circuit components. Changes in EC_{30} values reflect acquired resistance or sensitization. Data are presented as fold-change in EC_{30} (mean ± sd, n = 4 replicatesl). The sum-of-squares F-test was used to determine if selection treatment yields significantly altered dose-response curves from cells that did not undergo selection treatment: *p* value ≈ 0, F value = 141 for Sotorasib selection and challenge treatment; *p* value = 5×10^{-14}, F value = 43 for circuit selection and challenge treatment; *p* value ≈ 0, F value = 235 for Sotorasib selection and circuit challenge treatment; *p* value = 0.11, F value = 2 for circuit selection and Sotorasib challenge treatment.

Notably, circuits bypassed the need for oncogene addiction, remaining exceptionally potent across both Ras-addicted and non-addicted cells (**Figure 6d**). While NCI-H358 cells ($KRAS^{G12C}$) displayed Ras addiction and were sensitive to drugs, they were still killed more completely by the circuit. We also tested three Ras-mutant cell lines that do not exhibit Ras addiction: SW1573 (lung, $KRAS^{G12C}$), OV56 (ovary, $KRAS^{G12C}$), and PANC-1 (pancreas, $KRAS^{G12D}$). While these cells exhibited weak responses to drugs, they remained exceptionally sensitive to the circuit, which near-completely reduced their viabilities (**Figure 6d**). Further, to examine the durability of response, we analyzed the response of non-Ras addicted SW1573 cells to a single dose of drug or circuit over 1 week of continuous culture. The circuit, but not the drugs, durably eliminated these cells and prevented their recovery within this period (**Extended Data Figure 10b**).

Acquired resistance limits the clinical efficacy of targeted therapies such as Sotorasib[6,8]. To quantitatively compare the susceptibility of MIA PaCa-2 cells to acquired resistance under Sotorasib or circuit treatment, we performed three rounds of five-day selection at the EC_{70} of each treatment. We then challenged cells with another round of the same respective treatment to assess resistance (**Figure 6e**). Consistent with preclinical models and patient outcomes, Ras mutant MIA PaCa-2 cells rapidly acquired resistance, requiring 30-fold higher drug concentrations to reach the same cell killing efficiency (EC_{30}) post-selection compared to pre-selection (**Figure 6e**). In contrast, circuit selection increased circuit EC_{30} by only 1.3-fold. Moreover, Sotorasib's maximum killing efficiency dropped from ~75% in pre-selection cells to ~50% in post-selection cells, whereas the circuit maintained over 98% maximum efficiency post-selection (**Figure 6e**). These results indicate that MIA PaCa-2 cells are less susceptible to acquired resistance to the circuit compared to Sotorasib.

Finally, given the clinical challenge of Sotorasib resistance, we wondered whether cells with acquired Sotorasib resistance (generated above) would also exhibit resistance to the circuit, or *vice versa* (**Figure 6e**). Interestingly, Sotorasib-resistant cells required 2.5-fold lower concentrations of circuit mRNA-LNP to achieve the same killing efficiency (EC_{30}) as non-resistant cells (**Figure 6e**). We reasoned that this effect could be related to the known resistance mechanisms of increased Ras expression (or amplification), either of which could increase sensitivity to the circuit. To test this hypothesis, we transiently overexpressed $KRAS^{G12C}$ in MIA PaCa-2 cells and treated these cells with either Sotorasib or the circuit. Indeed, transient $KRAS^{G12C}$ overexpression slightly increased resistance to Sotorasib but enhanced sensitivity to the circuit (**Extended Data Figure 10c**). Together, these results highlight a fundamental difference in the resistance profile of drug and circuit-based

therapies and suggest that future therapeutic circuits could help treat patients resistant to Ras-inhibiting drugs.

Discussion

Our results demonstrate end-to-end development of therapeutic protein circuits that kill Ras-mutant cancer cells and treat tumors *in vivo*. In fact, despite the induced tumors analyzed here being aggressive and extremely difficult to treat, circuits still showed significant therapeutic benefit. The circuits designed here achieved comparable specificity and superior potency compared to state-of-the-art drugs, while being considerably easier and faster to design. What accounts for these advantages? First, unlike drugs, the sense-and-kill mechanism used by the circuits does not require oncogenic addiction and is less sensitive to complex and poorly understood heterogeneity (outside of the Ras gene itself) in cancer cell populations. Second, the ability to use proteins as sensors allows for large binding interfaces that can detect molecular features such as mutations that are otherwise challenging to drug. Third, circuits allow precise control of cellular responses, in this case through activation of pre-defined cell death programs.

Circuit therapeutics have other advantages as well. The circuits are genetically compact (*e.g.*, ~2kb for the pyroptosis circuit *v2-s*) and easily deliverable by LNP. From a safety point of view, the use of mRNA allows circuits to function transiently without permanent genome modification. Circuits also offer benefits compared to pyroptosis-inducing gasdermin agonists. Unlike these drugs, which broadly activate pyroptosis and could induce hyper-inflammation, circuits restrict its activation to cancer cells. Additionally, since circuits ectopically deliver gasdermins, they could overcome the observed problem of gasdermin silencing in tumor cells, which would render drugs ineffective[80–82].

The present circuits have several limitations. First, more *in vivo* studies will be required to comprehensively evaluate circuit function in cell- and patient-derived xenografts as well as in metastatic settings, in order to better understand their therapeutic potential across diverse Ras-driven cancers. In particular, it will be important to determine how apoptosis and pyroptosis should be balanced to maximize tumor clearance while minimizing potential toxicity from hyper-inflammation. Second, while the sensors respond to many Ras mutations, they do not respond equally to all. Future work could produce improved sensors with broader specificity or introduce mixtures of sensors for different Ras variants. Third, while intravenous LNP delivery can target some clinically relevant tissues, many other disease sites remain inaccessible[62,68,69]. This issue could be mitigated by intratumoral delivery (in the cancer context), or through emerging technologies like selective organ targeting (SORT) nanoparticles[62]. We note that the circuit paradigm effectively shifts the burden of specificity from the delivery method to the circuit itself, which could make circuits compatible with higher penetrance but less tissue-specific delivery methods. Fourth, a potential concern with any circuit that uses non-human proteins is immunogenicity. Here, we used a viral protease as a major component. In the future, however, similar circuits could be implemented with humanized protease variants or by altering the substrate specificity of human proteases[83].

Perhaps the most interesting aspect of therapeutic circuits is their programmability. Replacing the sensor in the current circuits could retarget them to other cancer drivers such as MYC, β-catenin, or other oncogenes. In fact, circuits do not need to respond to oncogenes at all, but could be designed to sense any protein or combination of proteins that provide an accurate signature of disease state.

Similarly, circuit outputs could also be broadened to include release of cytokines or activation of other therapeutic responses[13,83]. Together, these results establish a potent, specific, and programmable mechanism for treating cancer and other human diseases.

Methods

Plasmid construction

Plasmids were generated via Gibson Assembly (NEBuilder HiFi DNA Assembly Master Mix; New England BioLabs) or KLD cloning (T4 Polynucleotide Kinase, T4 DNA Ligase, DpnI, T4 DNA Ligase Buffer; Thermo Scientific). Gene fragments were sourced from Twist Bioscience or Integrated DNA Technologies (IDT), or PCR-amplified from existing laboratory plasmid constructs. IDT synthesized all PCR primers. Plasmids were purified (QIAprep Spin Miniprep Kit or Qiacube machine; Qiagen), normalized (Thermo Scientific NanoDrop 8000), and sequence-verified (Plasmidsaurus or Genewiz) prior to experimental use.

Tissue culture and cell lines

Most cell lines were obtained from ATCC and cultured under standard conditions (37°C, 5% CO2, humidified Eppendorf CellXpert C170i incubator). Adherent cells were maintained in Dulbecco's Modified Eagle Media (DMEM; Thermo Fisher) supplemented with 10% fetal bovine serum (FBS; Avantor), penicillin (1 unit/ml), streptomycin (1 µg/ml), glutamine (2 mM), sodium pyruvate (1 mM), and 1X Minimal Essential Media Non-Essential Amino Acids (all Thermo Fisher). HEK293FT cells were cultured for up to 20 passages, and human cancer cell lines for up to 15 passages, maintaining 10%-90% confluency. Cells were passaged using 0.25% Trypsin-EDTA (Thermo Fisher). Viable cell numbers for seeding densities were determined using Trypan Blue (Invitrogen) and the Countess 3 automated cell counter (Thermo Fisher). Cells were routinely confirmed mycoplasma-free (MycoStrip kit; InvivoGen). Cell lines with stably integrated fluorescent proteins used for microscopy were purchased from FenicsBIO.

Transient transfection

Transient transfections were performed utilizing FuGENE HD (Promega), Lipofectamine 3000 (Thermo Fisher), or LNPs (described below) as transfection agents. Unless otherwise noted, we seeded 10k cells (96-well plate), 200k cells (24-well plate) for FuGENE or LNP transfections, and 275k cells (24-well plate) for Lipofectamine transfections. Cells were reverse-transfected immediately after seeding following manufacturer instructions. For FuGENE transfections, we incubated 1 µg plasmid DNA with 6 µl transfection reagent. For FuGENE transfections, 200k cells were transfected with up to 566 ng of DNA. For Lipofectamine transfections, 1.5 µl Lipofectamine 3000 and 1.5 µl reagent P3000 were used with a total of 500 ng DNA to transfect an equivalent of 275k cells. The total amount of plasmid DNA applied in each transfection was scaled according to seeding densities.

Flow cytometry

Cells were collected two days post-transient transfection for flow cytometry, filtered through a 40-µm cell strainer, and analyzed by flow cytometry (CytoFLEX S flow cytometer, Beckman Coulter). Unless otherwise noted, we used FITC-A channel (GFP of iTEVP reporter[54]; excitation 488 nm, emission 525/40 nm; gain of 1), ECD-A channel (mRuby3; excitation 561 nm, emission 610/20 nm; gain of 1), PB450-A channel (mTagBFP2; excitation 405 nm, emission 450/45 nm; gain of 1), and APC-A700-A

channel (IFP of iTEVP reporter; excitation 638 nm, emission 712/25; gain of 100). Live cells and singlets were gated using FlowJo (version 10.10, BD Biosciences). iTEVP reporter activation was assessed by calculating the IFP (activation) to GFP (reporter expression) ratio for cells with GFP expression between 10^5 and 10^6 a.u., corresponding to the reporter expression regime with maximal dynamic range. As the reporter construct was always transfected as a separate polytransfection mix, selecting cells with high reporter expression did not bias subsequent analysis steps, *i.e.*, the expression distribution of other constructs (*e.g.*, reporter or ectopic Ras) remained unaffected.

Computational identification of Ras binding domains

To identify candidate Ras binding domains, we first extracted human proteins known to physically associate with KRAS from the STRING database[84] (physical subnetwork, medium confidence). All proteins passing these filters were co-folded with wild-type KRAS-4B and GTP using AlphaFold3 (AlphaFold Server)[85]. Binders predicted to interact with the CAAX domain of KRAS-4B were manually removed. To identify candidate binders for experimental characterization, we filtered for binders with high-confidence Ras interactions (interface PAE score < 10 and interface plDDT score > 75) and manually extracted Ras-interacting domains from the full-length proteins. For the proteins ARAF, RAF1, RGL1, and RASA4 we generated multiple candidate binder versions corresponding to different truncations or domains of the full-length protein. We also mutated sequence regions known to act as nuclear localization signals (NLS). Furthermore, we used RFdiffusion[86] (*Base_ckpt* and *Complex_beta_ckpt* model with default parameters; no hotspot residue selection) to *de novo* design Ras binders between 50 and 100 amino acids in length. Briefly, target structures (KRAS, HRAS, NRAS including GTP or analog nucleotide as ligand) were obtained from the Protein Data Bank (PDB)[87]. PBD assemblies were filtered and processed to provide a single Ras domain as input for RFdiffusion. Sequence design was performed with ProteinMPNN-FastRelax (*dl_binder_design* pipeline)[88,89]. After co-folding candidate binders with their corresponding target using AlphaFold2[90] (*dl_binder_design* pipeline), binders were filtered for high-confidence Ras interactions (interface PAE score < 10 and interface plDDT score > 80). Binders with high likelihood of dimerization in the absence of Ras were removed (co-folding of binder homodimers with AlphaFold3). In parallel, we compiled a list of synthetic Ras-binding domains such as monobodies[49], DARPins[50,51], synthetic proteins[52], and nanobodies[53] from the available literature. All sequences were codon-optimized for expression in human cells (Genscript).

Sensor screening

To evaluate the sensitivity and specificity of candidate Ras sensors, we reverse transfected HEK293FT cells (275k seeding density) with three separate plasmid mixes encoding (1) binder-cTEVP (120 ng), binder-nTEVP-IRES-mTagBFP2 (150 ng); (2) wild-type or mutant Ras (15 ng), mRuby3 (45 ng); and (3) iTEVP reporter fused to a CAAX membrane tether (170 ng). Transfections were performed with Lipofectamine 3000 according to the manufacturer's instructions. To characterize the binders, we gated for medium sensor (mTagBFP2 expression between 10^4 and 10^6 a.u.) and high Ras expression (mRuby3 expression between 10^5 and 10^6 a.u.). To analyze sensor responses to varying amounts of Ras, we gated for medium sensor expression (mTagBFP2 expression between 10^4 and 10^6 a.u.) and binned Ras expression as shown in plots. All plots show median reporter activation for the corresponding gate or bin. Confidence estimates for sensor

screening experiments were obtained by bootstrapping (95% confidence intervals; 1,000 bootstrap iterations).

Sensor targeting scope characterization

To evaluate the targeting scope of Ras sensors, we tested the sensor performance against a list of Ras variants compiled by selecting all KRAS, HRAS, and NRAS variants from the TCGA pan-cancer database (accessed via the cbioportal server) that are present in at least 10 cancer patients[55,56]. Analog to our sensor screening procedure, we reverse transfected HEK293FT cells (200k seeding density) with three separate plasmid mixes encoding (1) binder-cTEVP (133 ng), binder-nTEVP-IRES-mTagBFP2 (180 ng); (2) wild-type or mutant Ras (13 ng), mRuby3 (40 ng); and (3) iTEVP reporter fused to a CAAX membrane tether (200 ng). Transfections were performed with FuGENE HD according to the manufacturer's instructions. To calculate the fold-change of the response to mutant vs. wild-type Ras, we gated for medium sensor (mTagBFP2 expression between 10^4 and $10^{5.5}$ a.u.) and high Ras expression (mRuby3 expression between 10^5 and 10^6 a.u.) and divided the median activation to a given mutant Ras variant to the median activation to the corresponding wild-type Ras isoform. Confidence estimates were obtained by bootstrapping (95% confidence intervals; 1,000 bootstrap iterations).

Single-cell classification performance of sensors

To evaluate the ability of our sensors to discriminate between wild-type (WT) and mutant Ras proteins at the single-cell level, we conducted receiver operating characteristic (ROC) curve analysis. First, we selected all cells with medium sensor (mTagBFP2 expression between 10^4 and $10^{5.5}$ a.u.) and high Ras expression (mRuby3 expression between 10^5 and 10^6 a.u.). Next, for each sensor, we compared normalized reporter activation between cells expressing mutant Ras variants and those expressing the corresponding wild-type proteins. Normalized activation was calculated as the ratio of the iTEVP activation signal to the iTEVP expression level (IFP/GFP). ROC curves were generated for each sensor by setting thresholds across the range of observed normalized reporter values. At each threshold, we classified cells into true positives (mutant cells above threshold), false positives (wild-type cells above threshold), true negatives (wild-type cells below threshold), and false negatives (mutant cells below threshold). The true positive rate (sensitivity) and false positive rate (1 - specificity) were calculated accordingly. The area under the ROC curve (AUC) was determined using the trapezoidal rule, providing a quantitative measure of each sensor's discriminatory performance. Higher AUC values indicated better sensor performance in distinguishing mutant from wild-type Ras proteins.

Sensor characterization in human cancer cell lines

To characterize the performance of sensors in human cancer cell lines, we reverse transfected 250k cancer cells in a 24 well plate with two separate plasmid mixes encoding (1) binder-cTEVP (100 ng), binder-nTEVP-IRES-mTagBFP2 (135 ng); and (2) iTEVP reporter fused to a CAAX membrane tether (150 ng). After 48h, cells were analyzed by flow cytometry. Median sensor activation was calculated as the ratio of the iTEVP activation signal to the iTEVP expression level (IFP/GFP). Confidence estimates were obtained by bootstrapping (95% confidence intervals; 1,000 bootstrap iterations). We

used the same setup to characterize single-protein sensors. Median reporter activity was calculated after gating for all sensor-transfected cells (mTagBFP2 expression between $10^{3.5}$ and 10^{6} a.u.).

Design and Screening of Protease-Activatable Proteases

We designed a panel of candidate protease-activatable proteases based on diverse natural and synthetic protein activation mechanisms. All constructs were expressed in HEK293 cells via transient transfection for characterization.

Candidates 1-3: To emulate autoinhibition-based activation mechanisms observed in proteins such as WASP, SNARE, and ERM, we designed constructs in which a non-cleavable, synthetic autoinhibitory peptide was tethered to the active site of TVMV protease (TVMVP)[47]. The tether included a cleavage site for an orthogonal protease (TEVP), enabling activation through proteolytic removal of the inhibitory domain. Constructs were tested with and without co-expression of the activating TEVP protease. To modulate inhibitory dynamics, we generated a series of variants with progressively shortened linkers between the autoinhibitory peptide and TVMVP.

Candidates 4-7: To improve autoinhibition, we developed a tethering strategy in which the autoinhibitory peptide was anchored at both termini via two TEVP cleavage sites. We circularly permuted the TVMVP sequence and rejoined the new termini using antiparallel leucine zippers to stabilize the conformation. To optimize access of TEVP to its cleavage sites, we also varied the length of the linker flanking the autoinhibitory domain.

Candidates 8-10: We next explored strain-based inhibition, drawing inspiration from previous studies where circular permutation introduces conformational strain that disrupts protein function (*e.g.*, CRISPR)[91]. We engineered circularly permuted variants of TVMVP in which the old termini were joined by short linkers, embedding the TEVP cleavage site to allow strain release upon protease input. Additional constructs included deletions of disordered residues at the native termini to increase the distance between ends and enhance strain potential.

Candidates 11-13: To sterically inhibit the TVMVP active site, we fused bulky de novo designed heterodimers to the protease, positioned to occlude the catalytic cleft[92]. These heterodimeric blocking domains were flanked by TEVP cleavage sites to enable conditional displacement and activation.

Candidates 14-18: We adopted a protease caging strategy using split TVMVP[13,38,92]. One protease half was caged by fusion to a catalytically inactive TVMVP fragment via designed coiled coils. The coiled coil associated with the inactive half was flanked by TEVP cleavage sites, enabling conditional release. Additional constructs extended this strategy by caging both protease halves with inactive TVMVP fragments, each released via TEVP cleavage. To enable protease activation through strand displacement, we substituted the coiled coils with lower-affinity, sequence-matched variants previously reported to allow displacement by higher-affinity interactors. These designs were intended to facilitate TEVP-dependent exchange of inhibitory domains with active TVMVP halves.

mRNA production

DNA templates containing a 5' T7 promoter sequence followed by the dinucleotide sequence AG were linearized by PCR (Q5 High-Fidelity DNA Polymerase, NEB). A 3' end 120-base pair polyA-tail was added using PCR. The linear DNA templates were purified by Ampure beads or gel purification

(Zymoclean Gel DNA Recovery Kit, Zymo). mRNA was subsequently produced via *in vitro* transcription (IVT) using NEB's HiScribe T7 High Yield RNA Synthesis Kit. The IVT reaction mix contained 10X Reaction Buffer (1X final), 1 µg DNA template, 4 mM CleanCap AG (TriLink), 2 µl T7 RNA polymerase mix, and the nucleotides ATP, GTP, CTP, and *N1*-Methyl-Pseudouridine-5'-Triphosphate (TriLink) at a final concentration of 5 mM. After an incubation period of 2 hours at 37 °C, DNAse I (NEB) was added and reactions were incubated for another 15 minutes at 37 °C. Finally, mRNA was purified using Zymo's RNA Clean and Concentrator Kit and concentrations were read out by Nanodrop or Qubit RNA High Sensitivity or Broad Range kits. The concentration normalized mRNAs were stored at -80 °C.

Lipid nanoparticle (LNP) mRNA encapsulation

We adopted a previously described 4 component LNP formulation[63] (4A3-SC8, DOPE, Cholesterol, DMG-PEG) that enables transfection of cells in culture and *in vivo*.

To prepare the lipid stock solutions, a full 25 mg tube of 4A3-SC8 compound was dissolved in 167 µL of pure ethanol to yield a 150 mg/mL stock solution. Separately, 10 mg of DOPE was dissolved in 1.0 mL of pure ethanol to produce a 10 mg/mL stock solution (alternatively, 100 mg in 10 mL ethanol). Similarly, 10 mg of cholesterol was dissolved in 1.0 mL of pure ethanol (or 50 mg in 5 mL ethanol), and 10 mg of DMG-PEG was dissolved in 1.0 mL of ethanol (or 50 mg in 5 mL ethanol), resulting in 10 mg/mL stock solutions for each. A 20 mM working lipid mixture was prepared by combining 6.7 µL of the 4A3-SC8 solution (23.8%, 4.76 mM), 50.7 µL of the DOPE/DSPC solution (23.8%, 4.76 mM), 52.7 µL of the cholesterol solution (47.6%, 9.52 mM), and 34.2 µL of the DMG-PEG solution (4.8%, 0.96 mM).

The working lipid mixture was used to encapsulate mRNAs in the lipid nanoparticle (LNP) formulation. Initially, the lipid mixture was equilibrated at room temperature for at least 5 minutes and then vortexed at speed 10 for 5 seconds. A lipid mastermix was subsequently prepared by mixing 12 µL of the lipid mixture with 18 µL of 200-proof ethanol, yielding 30 µL per reaction. This mastermix was distributed into individual tubes. Each RNA mixture was prepared by combining 40 µL of RNA solution (250 ng/µL; total 10 µg RNA input) with 32 µL of nuclease-free water and 18 µL of 50 mM citrate buffer, yielding a total volume of 90 µL per reaction. To assemble the LNPs, 30 µL of the lipid mastermix was placed on a Vortex-Genie 2 vortex mixer set at speed level 1. While vortexing, 90 µL of the RNA mixture was rapidly pipetted into the lipid mastermix in a single action, and vortexing was continued for 30 seconds.

The resulting dispersion was incubated at room temperature for 5 minutes, and dialysis was initiated within 15 minutes of mixing. Dialysis was performed using Pur-A-Lyzer Midi 3500 dialysis tubes. Each tube was preconditioned by adding 900 µL of water, incubating for 5 minutes, and then removing the water. Approximately 120 µL of each LNP sample was transferred into the dialysis tubes, which were placed into a styrofoam holder and submerged in 1X PBS within a beaker. Dialysis was conducted either for 1 hour at room temperature or overnight at 4°C. After dialysis, each sample was transferred into an RNase-free 1.5 mL microcentrifuge tube, and the final volume was measured. Samples were adjusted to a total volume of 500 µL by adding the appropriate volume of 1X PBS. All samples were stored at 4°C.

The resulting mRNA-LNP particles exhibited nearly complete transfection efficiency of human MIA PaCa-2 cells, and allowed titration of expression over four orders of magnitude (**Extended Data Figure 6a**). This approach was also compatible with multi-component delivery of separately encapsulated mRNAs **(Extended Data Figure 6b**).

mRNA-LNP transfection of human cell lines

LNPs were reverse transfected by first adding LNPs to culture plates, followed by the addition of cells on top. To maximize transfection efficiency *in vitro*, mRNA-containing LNPs were pre-complexed with ApoE, a naturally excreted liver protein that binds lipids in vivo and recruits lipid particles to cells expressing the low-density lipoprotein (LDL) receptor.

Cell viability assay with CellTiter-Glo

Cell viability was assessed using the CellTiter-Glo (CTG) Luminescent Cell Viability Assay (Promega). Cells were seeded into 96-well plates at 100 µL medium per well and incubated with treatments as described for each experiment. Nunc Edge 2.0 plates were used to minimize edge effects. On the day of the viability assay, plates were removed from the incubator and equilibrated at room temperature for 30 minutes prior to CTG reagent addition. Subsequently, 100 µL of CTG reagent was directly added into each well. Plates were then placed on an orbital shaker in the Promega GloMax instrument and shaken for 2 minutes to facilitate cell lysis and thorough mixing of the reagent. Following shaking, plates were incubated at room temperature for an additional 10 minutes to stabilize the luminescent signal. During this incubation, 180 µL of the mixture from each well was transferred into a white luminescence-compatible plate. Luminescence was measured using the GloMax according to the manufacturer's protocol. Cell viability was calculated by normalizing raw luminescence measurements of treated to untreated samples. Where applicable, dose-response curves were modeled with a four-parameter log-logistic model. The same model was used to calculate EC_{30}, EC_{50}, EC_{70}, and EC_{90} concentrations. We compared the goodness of fit between different models with the sum-of-squares F-test. More specifically, we compared models fitting separate curves or a reduced four-parameter log-logistic model assuming a single curve.

Cell viability assay with flow cytometry

Cell Titer Glo (CTG) provides accurate measurements only within a specific range of cell densities. Thus, for experiments testing varying initial cell densities and their effects on drug versus circuit efficacy, we used flow cytometry to quantify cell viability. Annexin V staining was used to gate and exclude dead cells from analysis.

Analysis of Ras circuit response to EGF

HEK293 cells (100k cells per well) were seeded in a 24-well plate and treated with epidermal growth factor (EGF) at concentrations of 0, 0.1, 1, 10, and 100 ng/mL for 1 hour. Following treatment, cells were processed for phospho-ERK staining and analyzed by flow cytometry. Specifically, cells were fixed by adding an equal volume (600 µL) of 2X eBioscience™ IC Fixation Buffer directly to each well, followed by gentle vortexing to mix thoroughly. Samples were incubated for 20 minutes at room temperature in the dark. After fixation, cells were scraped thoroughly from each well using a pipette

tip, collected, and centrifuged at 600 × g for 5 minutes at room temperature, followed by removal of the supernatant. Cell pellets were then resuspended in the residual volume and permeabilized by adding 200 µL ice-cold 90–100% methanol (HPLC grade), followed by vortexing and incubation for at least 30 minutes on ice. Subsequently, cells were washed by adding 600 µL eBioscience™ Flow Cytometry Staining Buffer, centrifuged at 600 × g for 5 minutes, and the supernatant discarded. The wash step was repeated, leaving approximately 100 µL of residual staining buffer. Cells were stained with 5 µL (0.125 µg) directly conjugated anti-phospho-ERK1/2 antibody (Catalog #12-9109-42) for 30 minutes at room temperature in the dark. After staining, cells underwent two additional washes with 600 µL Flow Cytometry Staining Buffer, each followed by centrifugation at 400–600 × g for 4–5 minutes, with final resuspension in 100 µL of staining buffer for analysis. Finally, cells were analyzed by flow cytometry using the entire remaining volume (100 µL). The fraction of pERK positive cells was calculated as the fraction of cells with ECD-A signal > 10^3 a.u. Cell viability was measured as described above.

mRNA sequencing and analysis

mRNA was extracted from 96-well plates using Direct-zol-96 RNA Kits (Zymoresearch Cat# R2055). 50 ng of extracted mRNA from each sample was used as input for downstream NGS library preparation. mRNA-seq libraries were prepared in 96-well format using a modified 3'Pool-seq protocol. In brief, reverse transcription reactions were prepared by mixing input RNA with 1 µl Indexed RT Primer (10 µM), 1 µl 10 mM dNTP Mix (New England Biolabs Cat# N0447S), 1 µl diluted ERCC Spike-In Mix 1 (0.004 µL stock ERCC per µg RNA, ThermoFisher Cat# 4456740), 3.6 µl of 5X RT buffer (ThermoFisher Cat# EP0752), 0.5 µl of RNase inhibitor (ThermoFisher Cat# EO0381), 1 µl Maxima RT H Minus (ThermoFisher Cat# EP0752), and 2.5 µl 10 µM Template Switching Oligo in an 18 µl reaction. Reverse transcription was carried out in a thermocycler using the program described in the 3'Pool-seq protocol. Samples from each row of the 96-well plate were pooled (column pooling) by mixing an equal volume of each reverse transcription reaction into a new well, for a total volume of 20 µl. Residual primers were degraded by adding 1 µl Exonuclease I (New England Biolabs) and incubating at 37 °C for 45 min, followed by denaturation at 92 °C for 15 min. Subsequent cDNA amplification, tagmentation, and row pooling were performed following the 3'Pool-seq protocol. Finally, 20 µl of pooled NGS library was subjected to gel-based size selection using E-Gel EX Agarose Gel (ThermoFisher Cat# G401001) to enrich for fragments in the 200–1000 bp range, and eluted in 15 µl. Eluted pooled NGS libraries were examined using an Agilent TapeStation 4200 (Agilent Technologies) to determine average fragment sizes. Library concentration was quantified using a Qubit 3.0 Fluorometer (Life Technologies). NGS libraries were diluted to 2 nM, denatured in 0.2 N NaOH, and loaded onto the Element AVITI sequencer following the Element Biosciences Cloudbreak Sequencing user guide. Read de-multiplexing was performed with Bases2Fastq, a standard software package used with the Element Biosciences system. De-multiplexed reads were aligned to the reference genome GRCh38.103 using STAR (2.7.8a) with the ENCODE standard options, except "–outFilterScoreMinOverLread 0.3 –outFilterMatchNminOverLread 0.3 –outFilterMultimapNmax 20". Uniquely mapped reads that overlapped with genes were counted using HTSeq-count (0.13.5) with default settings, except "-m intersection-strict". To normalize for differences in sequencing depth across samples, we rescaled gene counts to counts per million (CPM). Fold-changes and adjusted p-values were calculated using the R package DESeq2.

Drug treatment *in vitro*

Cells were treated with Sotorasib/AMG-510 (10 mM, MedChemExpress, Cat. No.: HY-114277), RMC-7977 (10 mM, MedChemExpress, Cat. No.: HY-156498), or Paclitaxel (10 mM, MedChemExpress, Cat. No.: HY-B0015) at the indicated concentrations per experiment.

Time-lapse microscopy

HEK293 and MIA PaCa-2 cell lines were engineered to stably express mRuby3 and GFP, respectively. A co-culture containing 50,000 total cells at a 3:1 ratio of HEK293 to MIA PaCa-2 was seeded into black-walled, glass-bottom 24-well plates (Ibidi) and incubated overnight. The following day, drug or circuit treatments were applied, and plates were imaged using an Olympus automated microscope controlled by MetaMorph software. Time-lapse image acquisition was performed every 2 hours. Images were processed using a custom pipeline in Python. Raw image tiles were first stitched with 10% overlap to reconstruct full fields of view. Stitched images underwent three main processing steps. First, Gaussian filtering (7×7 kernel) was applied to denoise background speckles. Second, image contrast was normalized using percentile-based intensity scaling, with intensities rescaled between the 1st and 99.9th percentiles to account for field-to-field variation. Finally, a dual-threshold segmentation strategy was used for cell detection and quantification. Pixels exceeding the high threshold (20th percentile of the normalized intensity range) were classified as healthy cells and assigned a fixed intensity value of 180. Pixels between the high (20th percentile) and low (15th percentile) thresholds were preserved with their scaled intensities to capture cells with reduced fluorescence signal, indicative of potential cell stress or death. This method enabled consistent detection of both bright and dim cells while preserving biologically relevant signal variation.

Sequential resistance selection with drugs and circuit

MIA PaCa-2 cells were plated in a 10 cm tissue culture plate (350k cells/plate). Cells were treated with the IC_{70} concentrations that we previously determined, specifically 1 μM of Sotorasib and 60 pg/μL each of Ras sensor and Casp-3 mRNA-LNPs. After treatment for five days, cells were washed with PBS, trypsinized, replated at the same density (350k cells), and re-treated identically as described above. In total, cells underwent three rounds of selection treatment. At two time points—before the first treatment ("no selection") and after the final treatment—we collected cells and exposed them to concentration ranges of either Sotorasib or circuit. For Sotorasib, concentrations tested were 0.0001, 0.001, 0.01, 0.1, 1, and 10 μM. For circuit testing, cells were treated with mRNA-LNPs of Ras sensor/Casp-3 at concentrations of 10, 20, 40, 80, 160, and 320 pg/uL. Cell viability was read out by CellTiter Glo three days post transfection.

Analysis of Sotorasib and circuit response to increased Ras expression

10k MIA PaCa-2 cells were transfected with either 200 pg/μL $KRAS^{G12C}$ mRNA-LNP or 200 pg/μL NeoR mRNA-LNP as negative control. These mRNA-LNPs were co-delivered with 0.0001, 0.001, 0.01, 0.1, 1, and 10 μM of Sotorasib or 10, 20, 40, 80, 160, and 320 pg/uL of circuit mRNA-LNP (sensor *v2-s* + Casp-3). Cell viability was read out by CellTiter Glo three days post transfection.

Animal studies

All animal handling, care, and treatment procedures were carried out in accordance with the applicable regulations and guidelines established by the relevant Institutional Animal Care and Use Committee (IACUC). Animals were housed in polycarbonate cages within an environmentally controlled, well-ventilated room maintained at a constant temperature of 20-26°C and a relative humidity of 40-80%. Fluorescent lighting was provided on a 12-hour light/dark cycle.

In vivo hydrodynamic tail vein injection liver tumor models

FVB/NJ mice (Jackson Laboratory, 001800) were used for HDT tumor models due to their enhanced susceptibility to tumor development. The FVB mice used in this study were ordered directly from Jackson Laboratoriy (001800). Hydrodynamic transfection was used to introduce transposable vectors expressing mutant NRAS-G12V, TP53 shRNA, and sleeping beauty transposase (SB100) into FVB mice. Mice were injected at 6-8 weeks of age, when their body weights were ~18-25 g. HDT plasmids were suspended at the noted concentrations in 2 mL of saline and administered via tail-vein injection over 7 seconds. A 10:1 mass ratio of combined HDT plasmids to SB100 transposase plasmid was used. In the genetic tumor rescue experiments PT2-NRAS-G12V was used, and 10 ug/mouse of each plasmid was added to the HDT volume. LNP studies substituted PT3-NRAS-G12V, and 1 ug of this plasmid/mouse was used due to increased tumor induction efficiency. In the *in vivo* mRNA-LNP experiments, LNPs were dosed at 1.5 mg total RNA per kg body weight dissolved in 0.2 mL PBS via the lateral tail vein at the noted time points.

Liver and body weight measurements

Animals were euthanized by cervical dislocation under isoflurane anesthesia. Livers were removed, weighed, and imaged at the time of sacrifice. Liver/body weight ratios were calculated as follows: (whole liver weight)/(intact body weight) × 100. Extracted livers were imaged (anterior and posterior view) and corresponding images were used to assess the surface tumor burden of each animal. More specifically, tumor nodules were annotated manually in a blinded fashion. Surface tumor burden was calculated as accumulated surface tumor area over anterior and posterior liver views.

Liver surface tumor area annotation and masking

Liver images were manually annotated for nodules by an independent annotator with no involvement in the study. The annotation process was blinded: image files were assigned numeric identifiers, and the annotator was not provided with any information regarding experimental conditions. Tumors were manually segmented using NimbusImage on a total of 284 images of mouse livers. Each image received three separate masks: (1) “white nodes” for tumors that appeared lighter than surrounding tissue, (2) “black nodes” for tumors that appeared darker, and (3) a whole-liver mask outlining the total liver area. Only abnormalities larger than approximately 1 mm were included. Both raised masses and regions of distinct discoloration were classified as nodules. Non-tumor features such as fat deposits, blood vessels, bubbles, and specular reflections were excluded from annotation.

Kaplan-Meier curve

Tumors were induced in FVB mice as described above, with or without the noted circuits plasmids. Tumor development was allowed to proceed until reaching any of the three following clinical endpoints: a body condition score of 1, difficulty breathing, or decreased motility resulting in inability to obtain food or water, at which point mice were immediately euthanized at the recommendation of veterinary staff. Log-rank test was used to determine if differences in survival were significant.

LNP formulation and physical characterization for mouse studies

The following lipids were dissolved in 100% ethanol at a 15:30:15:3:7 molar ratio: 4A3-SC8 lipid (synthesized in-house), cholesterol (Sigma Aldrich Cat. No. C3045), DOPE (Avanti Polar Lipids Cat. No. 850725), DMG-PEG-2000 (Avanti Polar Lipids Cat. No. 880151), and DOTAP (Avanti, 890890P) with a total lipid:RNA mass ratio of 40:1. RNA was dissolved in 10 mM citrate buffer (pH 4.5) at a 3:1 v/v aqueous:organic phase ratio. LNPs were formed by microfluidic mixing of the lipid and RNA solutions using a Precision Nanosystems NanoAssemblr Benchtop Instrument, in accordance with the manufacturer's protocol. LNPs were dialyzed in PBS overnight at 4°C and stored at 4°C for up to 72 hours. Particle size and dispersity were measured by dynamic light scattering (DLS) using a Malvern Zetasizer DLS instrument.

Software

The following software was used in this study: PyMol, ChimeraX, FlowJo, AlphaFold 3, Colabfold (AlphaFold 2), RFdiffusion, ProteinMPNN-FastRelax (*dl_binder_design*), SnapGene, Geneious, Python, R, Bases2Fastq (Element Biosciences), DESeq2, MetaMorph, NimbusImage.

Statistics and reproducibility

Unless otherwise noted, all experiments were conducted with three to four technical or biological replicates.

References

1. Sawyers, C. Targeted cancer therapy. *Nature* **432**, 294–297 (2004).
2. Punekar, S. R., Velcheti, V., Neel, B. G. & Wong, K.-K. The current state of the art and future trends in RAS-targeted cancer therapies. *Nature Reviews Clinical Oncology* **19**, 637–655 (2022).
3. Moore, A. R., Rosenberg, S. C., McCormick, F. & Malek, S. RAS-targeted therapies: is the undruggable drugged? *Nat. Rev. Drug Discov.* **19**, 533–552 (2020).
4. Perurena, N. & Cichowski, K. Finding the sweet spot: Targeting RAS in tumors while sparing normal tissue. *Cancer Cell* **42**, 943–945 (2024).
5. Isermann, T., Sers, C., Der, C. J. & Papke, B. KRAS inhibitors: resistance drivers and combinatorial strategies. *Trends Cancer* (2024) doi:10.1016/j.trecan.2024.11.009.
6. de Langen, A. J. *et al.* Sotorasib versus docetaxel for previously treated non-small-cell lung cancer with KRASG12C mutation: a randomised, open-label, phase 3 trial. *Lancet* **401**, 733–746 (2023).
7. Wasko, U. N. *et al.* Tumour-selective activity of RAS-GTP inhibition in pancreatic cancer. *Nature* **629**, 927–936 (2024).
8. Awad, M. M. *et al.* Acquired resistance to KRASG12C inhibition in cancer. *N. Engl. J. Med.* **384**, 2382–2393 (2021).
9. Mohanty, A. *et al.* Acquired resistance to KRAS G12C small-molecule inhibitors via genetic/nongenetic mechanisms in lung cancer. *Sci. Adv.* **9**, eade3816 (2023).
10. Xue, J. Y. *et al.* Rapid non-uniform adaptation to conformation-specific KRAS(G12C) inhibition. *Nature* **577**, 421–425 (2020).
11. Gao, X. J., Chong, L. S., Kim, M. S. & Elowitz, M. B. Programmable protein circuits in living cells. *Science* (2018) doi:10.1126/science.aat5062.
12. Chung, H. K. *et al.* A compact synthetic pathway rewires cancer signaling to therapeutic effector release. *Science (New York, N.Y.)* **364**, eaat6982 (2019).
13. Vlahos, A. E. *et al.* Protease-controlled secretion and display of intercellular signals. *Nat Commun* **13**, 912 (2022).
14. Xia, S. *et al.* Synthetic protein circuits for programmable control of mammalian cell death. *Cell* **187**, 2785–2800.e16 (2024).
15. Zou, X., Zhao, C., Beier, K. T., Kang, C.-Y. & Lin, M. Z. Rewiring oncogenic signaling to RNA vector replication for the treatment of metastatic cancer. *bioRxivorg* (2025) doi:10.1101/2024.12.30.630713.
16. Siciliano, V. *et al.* Engineering modular intracellular protein sensor-actuator devices. *Nat. Commun.* **9**, 1881 (2018).
17. Chen, Z. & Elowitz, M. B. Programmable protein circuit design. *Cell* **184**, 2284–2301 (2021).
18. Yang, X. *et al.* Engineering synthetic phosphorylation signaling networks in human cells. *Science* (2025) doi:10.1126/science.adm8485.
19. Dobrin, A., Saxena, P. & Fussenegger, M. Synthetic biology: applying biological circuits beyond novel therapies. *Integr Biol (Camb)* **8**, 409–430 (2016).
20. Morsut, L. *et al.* Engineering Customized Cell Sensing and Response Behaviors Using Synthetic Notch Receptors. *Cell* **164**, 780–791 (2016).
21. Slomovic, S. & Collins, J. J. DNA sense-and-respond protein modules for mammalian cells.

Nat. Methods **12**, 1085–1090 (2015).
22. Duhkinova, M., Crina, C., Weiss, R. & Siciliano, V. Engineering Intracellular Protein Sensors in Mammalian Cells. *J Vis Exp* (2020) doi:10.3791/60878.
23. Xie, Z., Wroblewska, L., Prochazka, L., Weiss, R. & Benenson, Y. Multi-input RNAi-based logic circuit for identification of specific cancer cells. *Science* **333**, 1307–1311 (2011).
24. Angelici, B., Mailand, E., Haefliger, B. & Benenson, Y. Synthetic Biology Platform for Sensing and Integrating Endogenous Transcriptional Inputs in Mammalian Cells. *Cell Rep* **16**, 2525–2537 (2016).
25. Stein, V. & Alexandrov, K. Synthetic protein switches: design principles and applications. *Trends Biotechnol* **33**, 101–110 (2015).
26. Wang, Q. *et al.* A bioorthogonal system reveals antitumour immune function of pyroptosis. *Nature* **579**, 421–426 (2020).
27. Zhang, Z. *et al.* Gasdermin E suppresses tumour growth by activating anti-tumour immunity. *Nature* **579**, 415–420 (2020).
28. Ostrem, J. M., Peters, U., Sos, M. L., Wells, J. A. & Shokat, K. M. K-Ras(G12C) inhibitors allosterically control GTP affinity and effector interactions. *Nature* **503**, 548–551 (2013).
29. Holderfield, M. *et al.* Concurrent inhibition of oncogenic and wild-type RAS-GTP for cancer therapy. *Nature* **629**, 919–926 (2024).
30. Jiang, J. *et al.* Translational and therapeutic evaluation of RAS-GTP inhibition by RMC-6236 in RAS-driven cancers. *Cancer Discov.* **14**, 994–1017 (2024).
31. Behranvand, N. *et al.* Chemotherapy: a double-edged sword in cancer treatment. *Cancer Immunology, Immunotherapy* **71**, 507–526 (2021).
32. van den Boogaard, W. M. C., Komninos, D. S. J. & Vermeij, W. P. Chemotherapy side-effects: Not all DNA damage is equal. *Cancers (Basel)* **14**, 627 (2022).
33. June, C. H., O'Connor, R. S., Kawalekar, O. U., Ghassemi, S. & Milone, M. C. CAR T cell immunotherapy for human cancer. *Science* **359**, 1361–1365 (2018).
34. Sterner, R. C. & Sterner, R. M. CAR-T cell therapy: current limitations and potential strategies. *Blood Cancer J* **11**, 69 (2021).
35. Chau, C. H., Steeg, P. S. & Figg, W. D. Antibody-drug conjugates for cancer. *Lancet* **394**, 793–804 (2019).
36. Beck, A., Goetsch, L., Dumontet, C. & Corvaïa, N. Strategies and challenges for the next generation of antibody-drug conjugates. *Nat. Rev. Drug Discov.* **16**, 315–337 (2017).
37. Orehek, S. *et al.* Cytokine-armed pyroptosis induces antitumor immunity against diverse types of tumors. *Nat. Commun.* **15**, 10801 (2024).
38. Fink, T. *et al.* Design of fast proteolysis-based signaling and logic circuits in mammalian cells. *Nature chemical biology* **15**, (2019).
39. Langan, R. A. *et al.* De novo design of bioactive protein switches. *Nature* **572**, 205–210 (2019).
40. Zhang, J. Z. *et al.* Computationally designed sensors detect endogenous Ras activity and signaling effectors at subcellular resolution. *Nat. Biotechnol.* (2024) doi:10.1038/s41587-023-02107-w.
41. Chen, Z. *et al.* A synthetic protein-level neural network in mammalian cells. *Science* **386**, 1243–1250 (2024).
42. Plaper, T. *et al.* Designed allosteric protein logic. *Cell Discov.* **10**, 8 (2024).
43. Gao, X. J., Chong, L. S., Ince, M. H., Kim, M. S. & Elowitz, M. B. Engineering multiple levels of

specificity in an RNA viral vector. *bioRxiv* 2020.05.27.119909 (2020) doi:10.1101/2020.05.27.119909.
44. Kitada, T., DiAndreth, B., Teague, B. & Weiss, R. Programming gene and engineered-cell therapies with synthetic biology. *Science* **359**, (2018).
45. Prior, I. A., Hood, F. E. & Hartley, J. L. The frequency of Ras mutations in cancer. *Cancer Res.* **80**, 2969–2974 (2020).
46. Chung, H. K. & Lin, M. Z. On the cutting edge: protease-based methods for sensing and controlling cell biology. *Nature methods* **17**, (2020).
47. Stein, V. & Alexandrov, K. Protease-based synthetic sensing and signal amplification. *Proc. Natl. Acad. Sci. U. S. A.* **111**, 15934–15939 (2014).
48. Fink, T. & Jerala, R. Designed protease-based signaling networks. *Curr. Opin. Chem. Biol.* **68**, 102146 (2022).
49. Spencer-Smith, R. *et al.* Inhibition of RAS function through targeting an allosteric regulatory site. *Nat. Chem. Biol.* **13**, 62–68 (2017).
50. Bery, N. *et al.* KRAS-specific inhibition using a DARPin binding to a site in the allosteric lobe. *Nat. Commun.* **10**, 2607 (2019).
51. Guillard, S. *et al.* Structural and functional characterization of a DARPin which inhibits Ras nucleotide exchange. *Nat. Commun.* **8**, 16111 (2017).
52. Wallon, L. *et al.* Inhibition of RAS-driven signaling and tumorigenesis with a pan-RAS monobody targeting the Switch I/II pocket. *Proc. Natl. Acad. Sci. U. S. A.* **119**, e2204481119 (2022).
53. Teng, K. W. *et al.* Selective and noncovalent targeting of RAS mutants for inhibition and degradation. *Nat. Commun.* **12**, 2656 (2021).
54. To, T.-L. *et al.* Rationally designed fluorogenic protease reporter visualizes spatiotemporal dynamics of apoptosis in vivo. *Proc. Natl. Acad. Sci. U. S. A.* **112**, 3338–3343 (2015).
55. Cerami, E. *et al.* The cBio cancer genomics portal: an open platform for exploring multidimensional cancer genomics data. *Cancer Discov.* **2**, 401–404 (2012).
56. Sanchez-Vega, F. *et al.* Oncogenic Signaling Pathways in The Cancer Genome Atlas. *Cell* **173**, 321–337.e10 (2018).
57. Zhao, Y. *et al.* Structural basis for replicase polyprotein cleavage and substrate specificity of main protease from SARS-CoV-2. *Proc. Natl. Acad. Sci. U. S. A.* **119**, e2117142119 (2022).
58. Denard, C. A. *et al.* YESS 2.0, a Tunable Platform for Enzyme Evolution, Yields Highly Active TEV Protease Variants. *ACS Synth. Biol.* **10**, 63–71 (2021).
59. Sanchez, M. I. & Ting, A. Y. Directed evolution improves the catalytic efficiency of TEV protease. *Nat. Methods* **17**, 167–174 (2020).
60. McIlwain, D. R., Berger, T. & Mak, T. W. Caspase functions in cell death and disease. *Cold Spring Harb. Perspect. Biol.* **5**, a008656 (2013).
61. Kumar, S. Caspase function in programmed cell death. *Cell Death Differ.* **14**, 32–43 (2007).
62. Cheng, Q. *et al.* Selective organ targeting (SORT) nanoparticles for tissue-specific mRNA delivery and CRISPR-Cas gene editing. *Nat. Nanotechnol.* **15**, 313–320 (2020).
63. Wang, X. *et al.* Preparation of selective organ-targeting (SORT) lipid nanoparticles (LNPs) using multiple technical methods for tissue-specific mRNA delivery. *Nat Protoc* **18**, 265–291 (2023).
64. Kolch, W., Berta, D. & Rosta, E. Dynamic regulation of RAS and RAS signaling. *Biochem. J.*

480, 1–23 (2023).
65. Kiyatkin, A. *et al.* Scaffolding protein Grb2-associated binder 1 sustains epidermal growth factor-induced mitogenic and survival signaling by multiple positive feedback loops. *J. Biol. Chem.* **281**, 19925–19938 (2006).
66. Coyle, S. M. & Lim, W. A. Mapping the functional versatility and fragility of Ras GTPase signaling circuits through in vitro network reconstitution. *Elife* **5**, (2016).
67. Boykevisch, S. *et al.* Regulation of ras signaling dynamics by Sos-mediated positive feedback. *Curr. Biol.* **16**, 2173–2179 (2006).
68. Hou, X., Zaks, T., Langer, R. & Dong, Y. Lipid nanoparticles for mRNA delivery. *Nat. Rev. Mater.* **6**, 1078–1094 (2021).
69. Masarwy, R., Stotsky-Oterin, L., Elisha, A., Hazan-Halevy, I. & Peer, D. Delivery of nucleic acid based genome editing platforms via lipid nanoparticles: Clinical applications. *Adv. Drug Deliv. Rev.* **211**, 115359 (2024).
70. Biller, L. H. & Schrag, D. Diagnosis and treatment of metastatic colorectal cancer: A review: A review. *JAMA* **325**, 669–685 (2021).
71. Martin, J. *et al.* Colorectal liver metastases: Current management and future perspectives. *World J. Clin. Oncol.* **11**, 761–808 (2020).
72. Zhou, H. *et al.* Colorectal liver metastasis: molecular mechanism and interventional therapy. *Signal Transduct. Target. Ther.* **7**, 70 (2022).
73. Tada, M., Omata, M. & Ohto, M. High incidence of ras gene mutation in intrahepatic cholangiocarcinoma. *Cancer* **69**, (1992).
74. Chen, X. & Calvisi, D. F. Hydrodynamic transfection for generation of novel mouse models for liver cancer research. *Am. J. Pathol.* **184**, 912–923 (2014).
75. Molina-Sánchez, P. *et al.* Cooperation between distinct cancer driver genes underlies intertumor heterogeneity in hepatocellular carcinoma. *Gastroenterology* **159**, 2203–2220.e14 (2020).
76. Hsieh, M.-H. *et al.* Liver cancer initiation requires translational activation by an oncofetal regulon involving LIN28 proteins. *J. Clin. Invest.* **134**, (2024).
77. Liu, J., Kang, R. & Tang, D. Correction: The KRAS-G12C inhibitor: activity and resistance. *Cancer Gene Ther* **30**, 1715 (2023).
78. Li, B. T. *et al.* Largest evaluation of acquired resistance to sotorasib in KRAS p.G12C-mutated non–small cell lung cancer (NSCLC) and colorectal cancer (CRC): Plasma biomarker analysis of CodeBreaK100. *Journal of Clinical Oncology* (2022) doi:10.1200/JCO.2022.40.16_suppl.102.
79. Sabnis, A. J. & Bivona, T. G. Principles of resistance to targeted cancer therapy: lessons from basic and translational cancer biology. *Trends in molecular medicine* **25**, 185 (2019).
80. Fontana, P. *et al.* Small-molecule GSDMD agonism in tumors stimulates antitumor immunity without toxicity. *Cell* **187**, 6165–6181.e22 (2024).
81. Oltra, S. S. *et al.* Distinct GSDMB protein isoforms and protease cleavage processes differentially control pyroptotic cell death and mitochondrial damage in cancer cells. *Cell Death Differ.* **30**, 1366–1381 (2023).
82. Kong, Q. *et al.* Alternative splicing of GSDMB modulates killer lymphocyte-triggered pyroptosis. *Sci. Immunol.* **8**, eadg3196 (2023).
83. Aldrete, C. A. *et al.* Orthogonalized human protease control of secreted signals. *bioRxiv*

2024.01.18.576308 (2024) doi:10.1101/2024.01.18.576308.
84. von Mering, C. *et al.* STRING: a database of predicted functional associations between proteins. *Nucleic Acids Res.* **31**, 258–261 (2003).
85. Abramson, J. *et al.* Accurate structure prediction of biomolecular interactions with AlphaFold 3. *Nature* **630**, 493–500 (2024).
86. Watson, J. L. *et al.* De novo design of protein structure and function with RFdiffusion. *Nature* 1–3 (2023) doi:10.1038/s41586-023-06415-8.
87. Berman, H. M. *et al.* The Protein Data Bank. *Nucleic Acids Res.* **28**, 235–242 (2000).
88. Dauparas, J. *et al.* Robust deep learning-based protein sequence design using ProteinMPNN. *Science* **378**, 49–56 (2022).
89. Bennett, N. R. *et al.* Improving de novo protein binder design with deep learning. *Nat. Commun.* **14**, 2625 (2023).
90. Jumper, J. *et al.* Highly accurate protein structure prediction with AlphaFold. *Nature* **596**, 583–589 (2021).
91. Oakes, B. L. *et al.* CRISPR-Cas9 circular permutants as programmable scaffolds for genome modification. *Cell* **176**, 254–267.e16 (2019).
92. Chen, Z. *et al.* Programmable design of orthogonal protein heterodimers. *Nature* **565**, 106 (2018).

Acknowledgements

We thank Duncan Chadly, Dongyang Li, Rongrong Du, Victoria Tobin, Martin Tran, Jacob Parres-Gold, Jan Gregrowicz, Evan Mun, Ron Hadas, Ethan Richman, Jordan Lay, Sean Hsieh, Nikita Makarov, Roey Lazarovits, and Arun Chakravorty for advice on experimental design, technical support, insightful discussions, or critical proofreading of the manuscript; Inna-Marie Strazhnik for graphical design; Leah Santat, Jo Leonardo, and Rui Malinowski for administrative support. This research was supported by the National Institutes of Health (*EB030015*) and the Mathers Foundation (*12540447*). The content is solely the responsibility of the authors and does not necessarily represent the official views of the National Institutes of Health. M.B.E. is a Howard Hughes Medical Institute Investigator. H.Z. is supported by the NIH R01 grants (*CA251928*, *AA028791*), and the Emerging Leader Award from the Mark Foundation For Cancer Research (*#21-003-ELA*). D.J.S. acknowledges support from the National Institute of Biomedical Imaging and Bioengineering (NIBIB, *R01 5R01EB025192-06*) and National Cancer Institute (NCI, *R01 CA269787-01*). A.L. is supported by the Paul & Daisy Soros Fellowship. S.X. is supported by the Jane Coffin Childs Memorial Fund for Medical Research and the Joan A. Steitz Fund. B.G. is supported by the Damon Runyon Fellowship (*DRG-2441-21*).

Author contributions

A.L., L.M., and M.B.E. conceived and designed the study. S.M., A.L., and L.M. conceived and designed *in vivo* experiments. M.B.E. directed and supervised the study. D.J.S., H.Z., and M.B.E. directed and supervised *in vivo* experiments. A.L., L.M., and K.K. performed *in vitro* and computational experiments. S.X., E.Z., M.W.B., H.L., A.A.D., J.M.L., M.J.F., and X.J.G. assisted with or offered guidance regarding *in vitro* or computational experiments. S.M. performed *in vivo* experiments. B.G. performed RNAseq experiments. L.K. manually annotated liver surface tumors. A.L., L.M., and S.M. analyzed data. A.L., L.M., and M.B.E. wrote the manuscript with input from all authors.

Competing interests

Patent applications related to this work have been filed by the California Institute of Technology. M.B.E. is a scientific advisory board member or consultant at TeraCyte, Plasmidsaurus, Asymptote Genetic Medicines, and Spatial Genomics. H.Z. is a co-founder of Quotient Therapeutics and Jumble Therapeutics, is an advisor for Newlimit and Alnylam Pharmaceuticals. D.J.S. discloses interests in ReCode Therapeutics, Signify Bio, Pegasus Bio, and Jumble Therapeutics. X.J.G is a co-founder of and serves on the scientific advisory board of Radar Tx. These interests are not directly relevant to this paper.

Data and code availability

Data needed to evaluate the conclusions are available in the paper, the extended data figures, or the Supplementary Materials. Raw data and computer code used for data analysis are available from the corresponding author upon request.

Materials and correspondence

All material requests and correspondence should be addressed to M.B.E.